2016

A SEARCH FOR MULTI-CHARGED HEAVY STABLE PARTICLES AT â^šs = 13 TeV

Austin Vihncent Skeeters

THE FLORIDA STATE UNIVERSITY

COLLEGE OF ARTS AND SCIENCES

A SEARCH FOR MULTI-CHARGED HEAVY STABLE PARTICLES AT $\sqrt{s} = 13$ TeV

By

AUSTIN VIHNCENT SKEETERS

A Thesis submitted to the
Department of Physics
in partial fulfillment of the requirements for graduation with
Honors in the Major

Degree Awarded:
Spring, 2016

The members of the Defense Committee approve the thesis of Austin Vihncent Skeeters defended on April 14, 2016.

Dr. Todd Adams
Thesis Director

Dr. David Kopriva
Outside Member

Dr. David Van Winkle
Committee Member

Dr. Bridget Alligood DePrince
Committee Member

Contents

List of Figures

List of Tables

Abstract

While not yet experimentally verified, many theoretical models of new physics allow for the existence of massive, long-lived particles exhibiting electric charges, Q, in excess of the elementary charge of the electron, e. A search for such multi-charged heavy stable charged particles (mHSCPs), specifically those characterized by charges in excess of e by integer multiples was performed utilizing $\sqrt{s}$ =13 TeV data from the Compact Muon Solenoid (CMS) detector at the Large Hadron Collider (LHC). mHSCPs display distinct signatures in the detector due to their slow speeds and large ionization energy depositions. Time of flight information was measured using the muon system, and ionization loss in the inner tracker. Due to readout saturation, techniques (cluster cleaning and cross talk inversion) have been developed to compensate for potential under-measurement of particle ionization. The objective of this investigation was to both place limits on mHSCP cross-sections, as well as to explore the effectiveness of cluster cleaning and cross-talk inversion. Experimentation resulted in cross section limits that increase with particle charge. Cluster cleaning and cross talk inversion together impose tighter cross section limits, suggesting a beneficial impact on the analysis as a whole, and warranting further investigation into other combinations of their applications.

Acknowledgements

I would like to thank Dr. Todd Adams for the countless hours of guidance and instruction that he has given me, as well as for affording me a tremendous level of independence during this project. Not many professors would come back to campus after five to listen to an undergraduate fumble through a presentation. I could not have asked for a better adviser.

Further thanks are extended to Andrew Ackert and Dr. Andrew Askew for answering any and all of my intelligent and not-so-intelligent questions.

A special thanks is necessary for my committee as well. Drs. Bridget DePrince, David Kopriva, and David Van Winkle who in their own unique ways spurred my interest in precision measurements and data analysis, abstraction of mathematical models, and physics education, respectively.

A last thanks goes to Dr. Kirby Kemper, who helped me to refine my presentation before presenting to Dr. Adams, and came to the rescue with his laptop.

1 Introduction

From antiquity through contemporary time mankind has zealously pursued a better understanding of the constituents of the world we they inhabit. Modern endeavors into this matter conducted under the field of particle physics are driven by two core tenets: All matter can be reduced to fundamental particles, and it is the interactions of those fundamental particles that dictate the evolution of the universe.

The Standard Model (SM) of particle physics serves as the current mathematical descriptor of the aforementioned, and agrees excellently with experimental data produced by the Large Hadron Collider (LHC) through high-energy proton-proton (pp) collisions. However, several disparities exist between reality and SM predictions, necessitating the advent of physics Beyond the Standard Model (BSM). Furthermore, the SM excludes the gravitational interaction altogether, suggesting a clear need for extension and refinement of the model. Many BSM theories that seek to remedy these disparities predict the existence of exotic particles, prime examples of which are multiply Charged Heavy Stable Charged Particles (mHSCPs) and Heavy Stable Charged Particle (HSCPs). The primary goal of this thesis is to conduct a search for mHSCPs, while refining data quality improvement techniques known as cluster cleaning and cross-talk inversion.

It is imperative that the validity of scientific models be experimentally verifiable and BSM theories are no exception. The LHC and its connected experiments allow for direct verification or exclusion of some theorized particles and interactions. By combining information from the various detector modules, signatures of possible mHSCP existence can be observed with the CMS detector. For the ensuing analysis, a heavily data-driven approach is utilized. Chapter 2 lays a basic BSM background. Chapter 3 describes the LHC and the CMS detector. Chapter 4 delves deeper into a discussion of calculated and observed variables of interest. Chapter 5 is dedicated to the offline (post data taking) analysis to search for mHSCPs both with and without cluster cleaning and cross-talk inversion turned on. Chapter 6 displays the results of the analysis and its potential implications.

2 Beyond the Standard Model

In order to adequately understand extensions to the Standard Model, it is necessary to present a working-knowledge explanation of the SM. The SM describes three of the four fundamental interactions known to man: electromagnetic, strong, and weak; with the excluded interaction being gravitational. All of matter is described in terms of these fundamental interactions, and the particles that mediate and experience them. A summary of these particles is given in Fig. 2.1.

2.1 Standard Model

Fermions, or matter particles with spin 1/2 interact by exchanging bosons, the spin 1 force carrier particles. The most well-known of these is the photon, the quanta of the electromagnetic interaction. There exist three "generations" of fermions, each with four particles: two leptons and two quarks. Oddly enough, it is only the first generation of these particles that constitutes all ordinary matter [1]. Each generation is characterized by different lifetimes, decay modes, and masses. Further, while many higher-generation particles will decay into lower generation ones (e.ġthe τ), some, such as the neutrinos, have no experimental evidence verifying decay of any kind. Any particle in the SM is also characterized by multiple quantum numbers including electric charge, color (strong

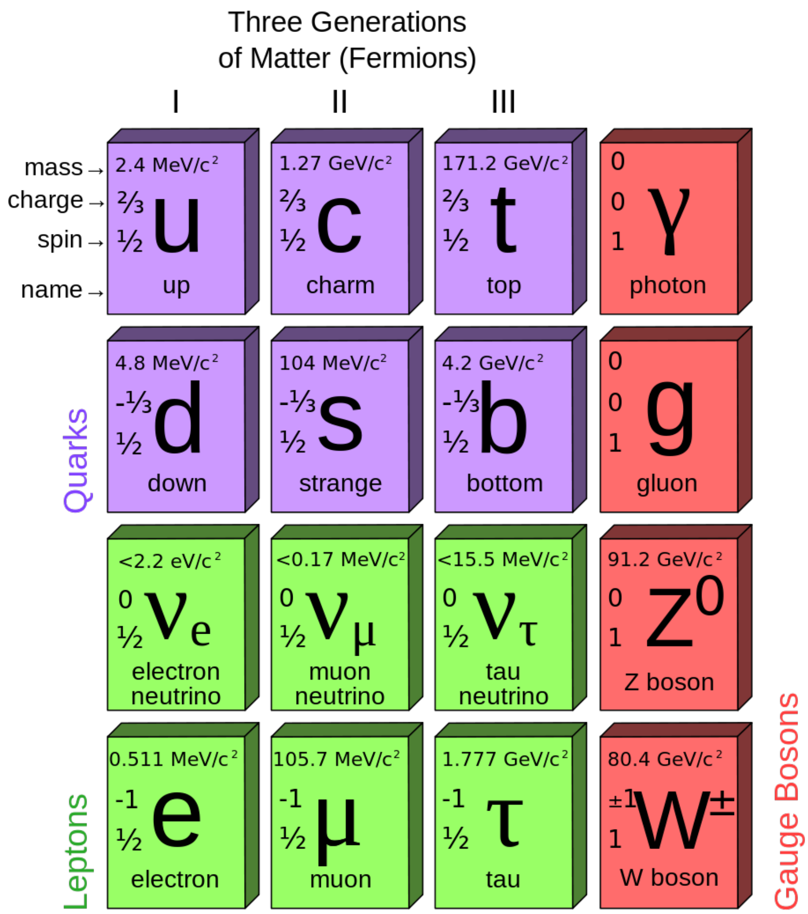

Figure 2.1: Tabulated representation of the Standard Model particle hierarchy (Higgs Boson not displayed)

charge), and Isospin (weak charge). Further, each lepton in the SM has a corresponding anti-particle of opposite quantum numbers.

Conservation of quantum numbers is imperative in determining particle stability. In this context, a "stable" particle refers to one that can be created and annihilated through the utilization of quantum mechanical operators. Stable particles must also satisfy the relativistic relationship between energy and mass: $E^2 = (pc)^2 + (mc^2)^2$ where E is the total energy of the particle, p is its momentum, m its rest mass, and c is the speed of light in vacuum. For example, the stability of the electron can be understood as a direct consequence of conservation of electric charge. The proton, a non-fundamental particle that is a combination of two up quarks and a down quark, receives its stability from conservation of baryon and lepton number [2]. Particle lifetime on the other hand can be heavily influenced by kinematic constraints alone. The neutron, for example, maintains a long lifetime due to a combination of the weakness of the interaction responsible for its decay, and the small difference in the masses of the proton and the neutron [3]. It would be sensible then to hypothesize that some new quantum number could be responsible for the stability of newly discovered, BSM particles.

2.2 HSCP & MCHSCP

BSM theories, Supersymmetry (SUSY) as an example, allow for Heavy Stable Charged Particles (HSCPs) as well as multi-charged HSCPs (mHSCPs). However, constraints are imposed on HSCPs based on experimental data and SUSY theory. The primary theoretical constraint comes in the form of a new SUSY quantum number known as R-parity, defined as:

$$\text{R-parity} = (-1)^{2S+3B+L} \tag{2.1}$$

with S being the particle spin, B its baryon number, and L its lepton number. Conservation of this quantum number leads to a stable particle, commonly referred to as the Lightest SUSY Particle, or LSP. The LSP must be neutral due to lack of observed electromagnetic interactions with non-SM properties. Thus, an HSCP can not be the LSP.

This search for HSCPs is most sensitive to particles with lifetimes on the order of microseconds to milliseconds. Muons traveling at roughly the speed of light take more than twenty nanoseconds to reach the muon system. Slower-moving HSCPs would therefore need to be much longer-lived in order for this analysis to be sensitive to them. A possible explanation for long HSCP lifetime is, at least in the hadron-like case, a consequence of it being in a bound R-hadron state.

While we have now established the feasibility of detecting HSCPs, we have yet to identify a mechanism by which they come into being. There are two primary types of HSCP: lepton-like, which exhibit electromagnetic and weak interactions but not strong, and hadron-like, involving supersymmetric quark and/or gluon bound states [4]. Q-balls, an example of the former, is a generic term for a large variety of baryonic and leptonic bound states. It is possible that they were created in the early universe through fluctuations resulting in aggregation of net charge in a spatial region, the smallest of which could be observed today in a detector as large as the CMS [3]. The latter is exemplified nicely by what is referred to as R-hadrons, formed as a consequence of the colored HSCPs which precipitate them. Shortly after a hadron-like HSCP is formed, the strong interaction (as this type of HSCP is colored) will cause it to hadronize, forming mesons (quark anti-quark bound states), baryons (three quarks), or glue-balls (bound gluon states devoid of quarks). More specifically though, R-hadrons consist of SM partons along with one heavy exotic parton, such as a gluino, $\tilde{g}$. Many BSM models assume that the exotic parton acts as a spectator during hadronic interactions with the detector, behaving as a reservoir for kinetic energy and leaving only a small fraction of the total energy available available for hadronic interaction. Therefore, both types of HSCP can be highly penetrating, leaving detector signals strongly resembling those of muons [4]. When detected though, HSCPs will be identified in a by a small $\beta = \frac{v}{c}$ (i.e. speed much slower than typically expected of SM particles.

3 Experimental Apparatus

The hardware utilized in this search consists of the LHC and the CMS detector. Counter-rotating proton beams in the LHC are accelerated to high energies and forced to collide at various interaction points around the main ring. Each interaction point is surrounded by a detector specifically designed to record particles from the interactions. Energy, momenta, and position are also measured as particles propagate through the detector material. By combining information from the detector segments concerning the precipitates of the initial interactions, the identity and properties of the initial reaction products can be discerned.

3.1 Large Hadron Collider

The LHC at CERN serves the primary purpose of accelerating counter-rotating proton beams to a nominal center-of-mass energy ($\sqrt{s}$) of 13 TeV [7]. The frequency of proton-proton interactions made possible by the LHC is roughly 10^9 per second, with a time-separation between proton bunches in the beam of roughly 25 ns. The main ring of the LHC is roughly 27 km in circumference, and housed in a tunnel up to 175 meters underground on the Franco-Swiss border.

Figure 3.1 depicts the overall layout of the CERN facilities. While it should be noted that

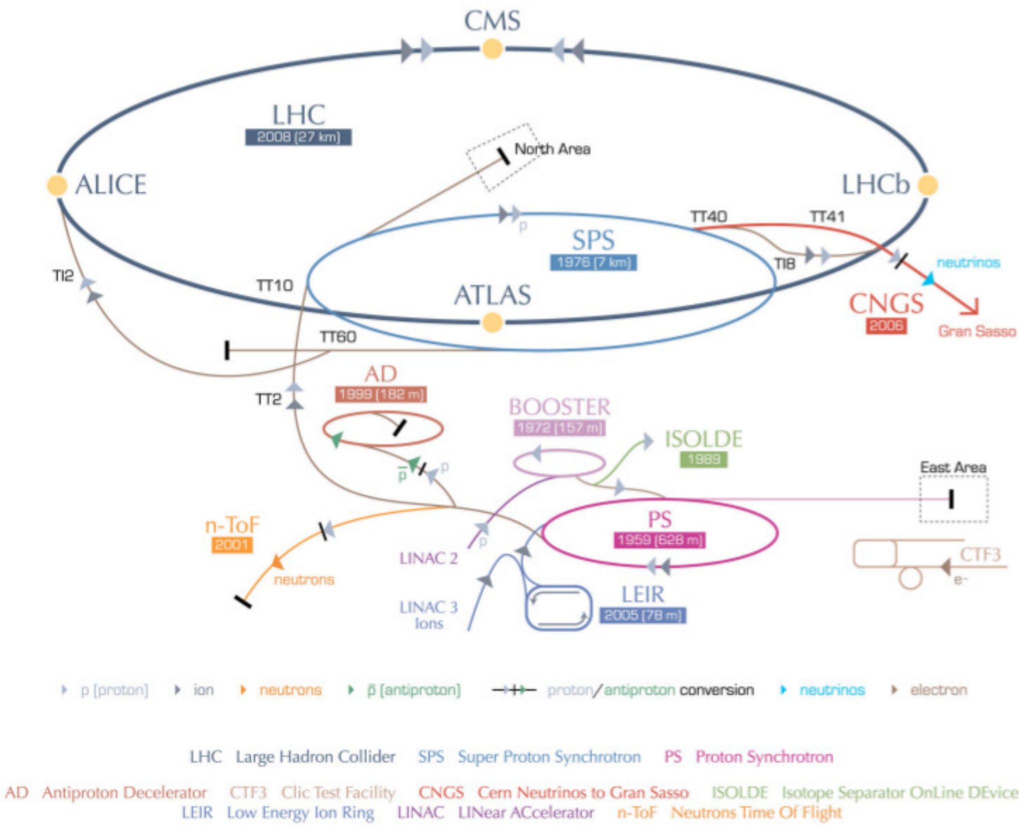

Figure 3.1: Schematic diagram of the CERN accelerator complex [8]

the protons are accelerated through several stages as shown near the bottom of Fig. 3.1, it is enough for the purposes of this analysis to recognize that by the time they reach their interaction points in the various detector, they are at the desired center-of-mass energy of 13 TeV. A more concise depiction of the LHC main ring and its attached detectors is shown in Fig. 3.2. Superconducting magnets cooled to 1.9 K by liquid helium as well as non-superconducting magnets are used to control the beams. Specifically, dipole magnets are used to keep the beams circulating in the beam pipes, and quadrupole magnets are used to focus them. Further specifications and technicalities can be found in [9] and [10].

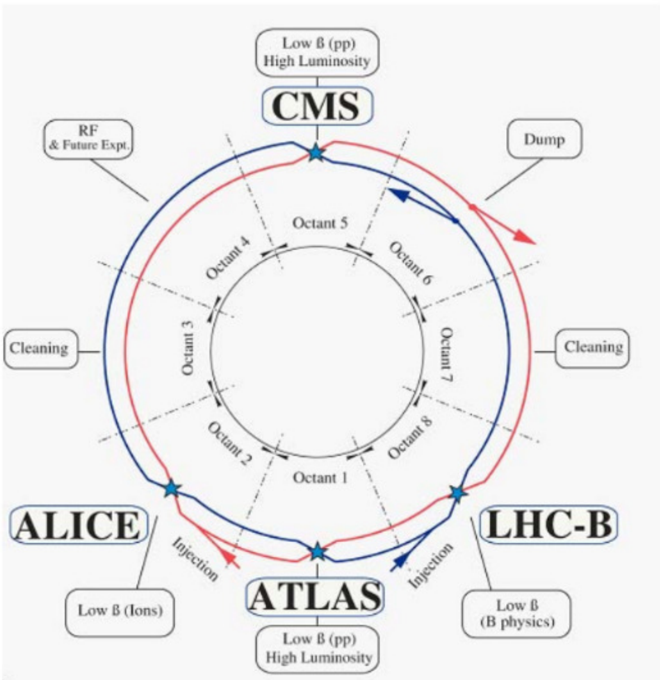

Figure 3.2: Schematic diagram of the LHC main ring [9]

A more complete description of the LHC is available in [10, 8]

The Compact Muon Solenoid (CMS) and A Toroidal LHC Apparatus (ATLAS) are general-purpose detectors capable of studying a wide range of physics, and marked by superb energy and position resolutions [11][12]. They are located in Octants 5 and 1, respectively, on Fig. 3.2. The granularity of these detectors, along with the synergy among their various components enable searches for BSM physics.

3.2 Compact Muon Solenoid Detector

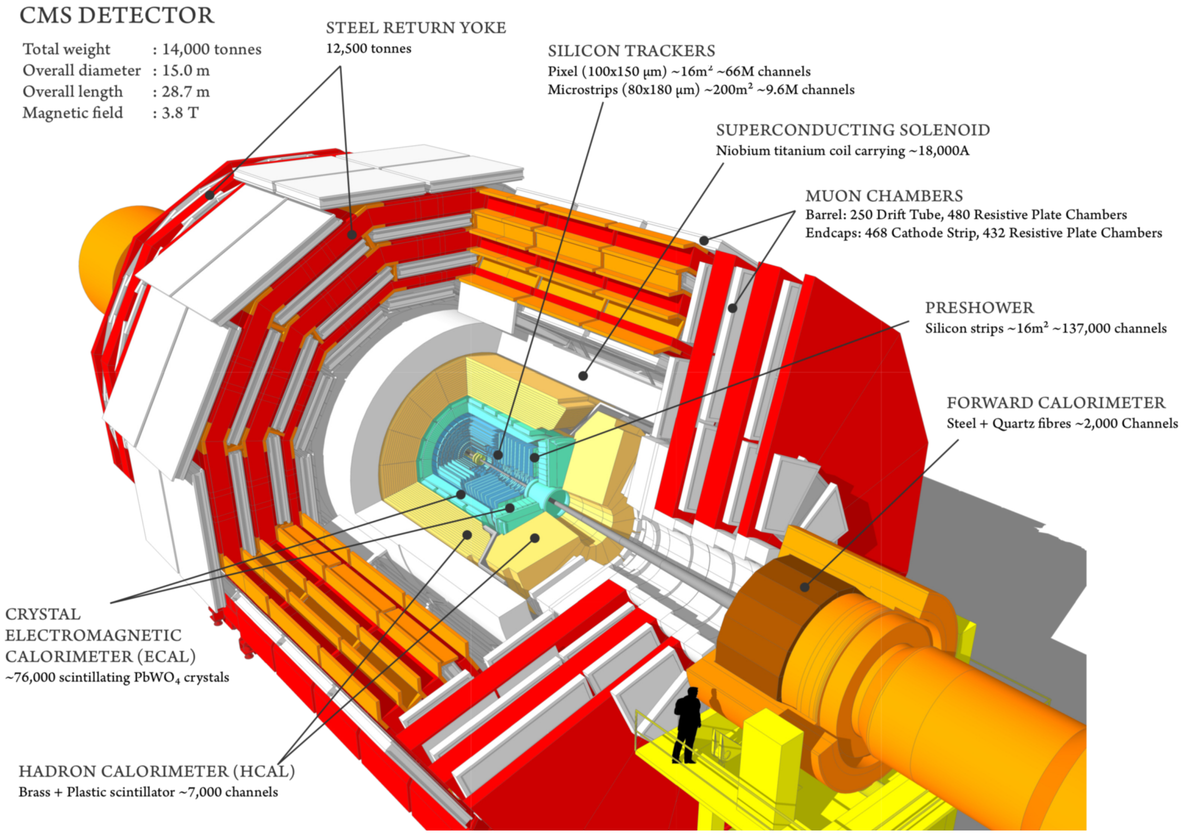

Figure 3.3: Schematic diagram of the CMS experiment [13]

The CMS detector has been specifically designed to maximize four criteria [11]: transverse momentum resolution(p_t), energy resolution (E), particle identification, and particle reconstruction. Depicted in Fig. 3.3, the CMS detector is a modular, solenoid-shaped detector 21.6 m long, and with a 14.6 m diameter. Ironically, although it is much smaller than the ATLAS detector (25 m, 7000 tons) in size, it weighs nearly twice as much (roughly 12500 tons). A 3.8 T superconducting solenoid provides sufficient bending power to accurately measure the momentum of high-energy particles based on their curvature. Further, combined information from the specialized detector segments allows for the accurate tracking and identification of incident particles.

3.2.1 Coordinates

Beginning with a Cartesian basis, the CMS coordinate system is measured from the nominal interaction point and has the x-axis pointing toward the center of the main LHC ring (Fig. 3.2), the y-axis pointing straight up orthogonal to the plane of the LHC, and the z-axis pointing along the beam line in the counterclockwise direction.

As is the case when describing a majority of physical systems, a Cartesian basis is not entirely useful, nor convenient for calculations. Further, it offers no conveniently calculable invariant for position that can be applied when boosting to different frames of reference. As such, it is more practical to utilize so called η (eta) ϕ (phi) coordinates.

We define the azimuthal angle, ϕ, to be the angle formed between the x-axis in the xy plane and the radial coordinate, r, projected into the plane. The radial coordinate corresponds physically to the particle's distance from the beam axis, z. The polar angle, θ, is measured from the positive beam (z) axis. The pseudorapidity, η, is defined as

$$\eta \equiv -\ln\left(\tan\frac{\theta}{2}\right)$$

which is an angular measure that is invariant under Lorentz boosts along the beam axis, as desired [14]. The η coverage of various segments of the CMS detector are depicted in Fig. 3.4.

Based on this coordinate system, it is useful to define a few physics variables of interest. Transverse momenutm, $\vec{p}_T \equiv \vec{p}\sin(\theta)$ is the component of momentum in the transverse (xy) plane. Similarly, transverse energy is defined as $E_T \equiv E\sin(\theta)$, where E is the deposited energy in the detector. E_T, $\vec{p}_T$, η, and ϕ together with an assumed $1e$ electric charge provide a complete description of the propagation of any particle through the CMS detector.

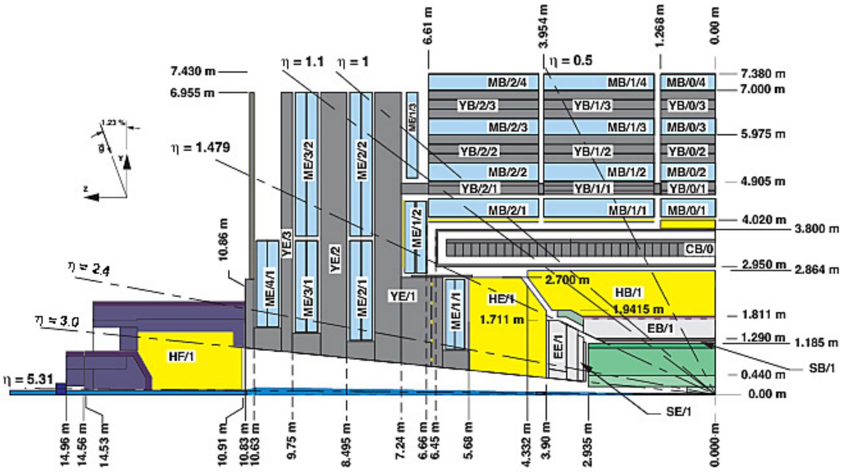

(a)

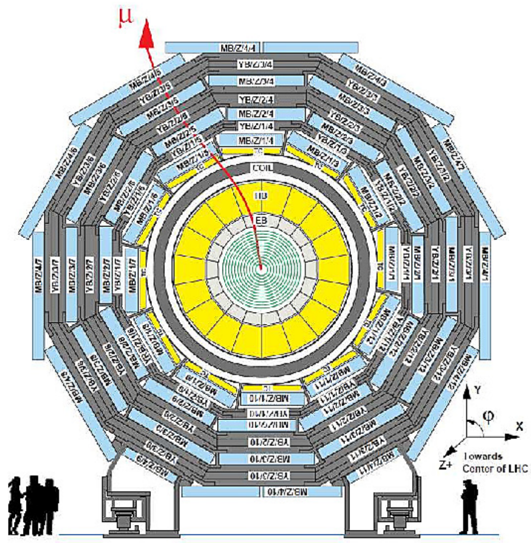

(b)

Figure 3.4: Schematic view of the CMS detector. The top figure (a) displays a longitudinal view of one quarter of the detector. The bottom figure (b) shows a transverse view at $z = 0$. The barrel muon detector elements are denoted as MBZ/N/S, where $Z = -2, ... + 2$ is the barrel wheel number, $N = 1...4$ the station number and $S = 1...12$ the sector number. Similarly, the steel return yokes are denoted YBZ/N/S [15]

3.2.2 Design/Layout

NOTE: Each of the following detector segments is visible in Fig. 3.5.

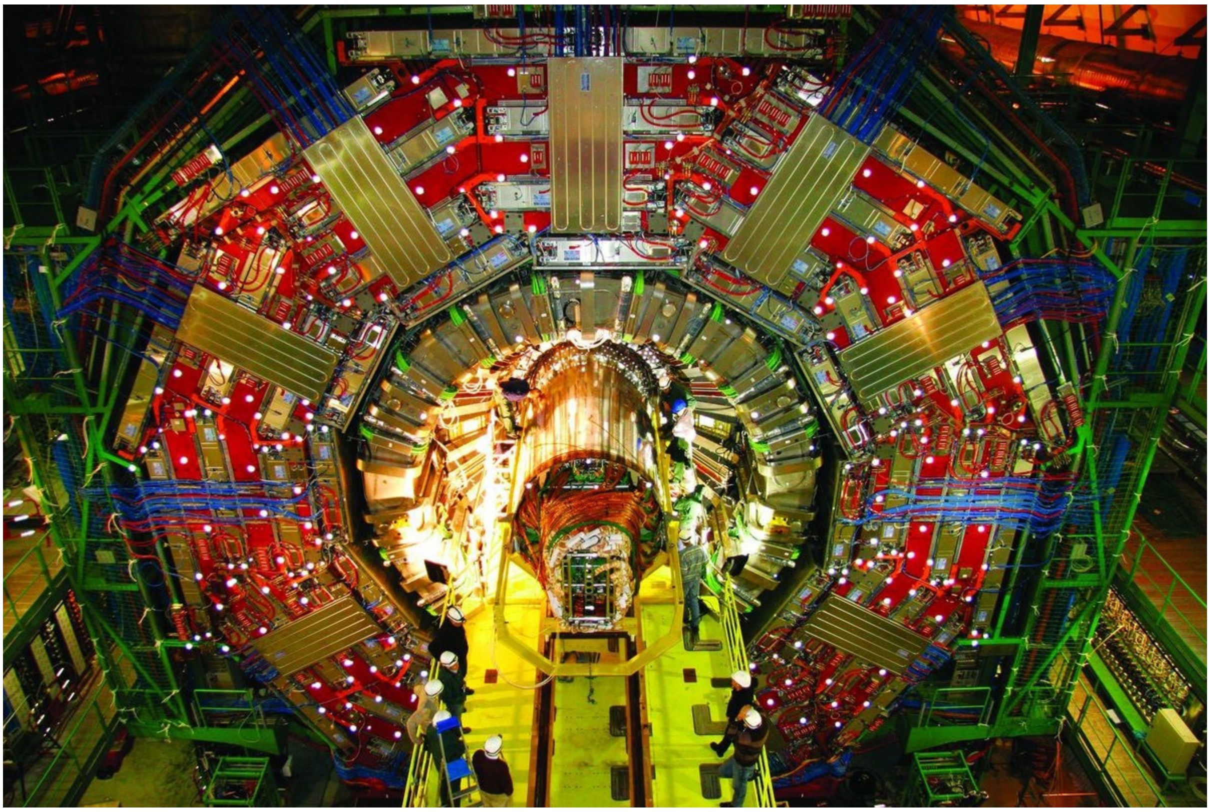

Figure 3.5: View of the CMS detector parallel to the beam axis

As displayed in Fig. 3.6, the CMS detector consists of cylindrical layers of sub-detector systems. Beginning with the closest component to the interaction point and branching out radially the detector is composed of the inner tracker, the electromagnetic calorimeter (ECAL), the hadronic calorimeter (HCAL), the superconducting solenoid magnet, and the muon detectors. The distinct feature of the CMS is its 3.8 T solenoid magnet of roughly 6 m internal diameter. All of the aforementioned components lie within the magnet, save for the muon system, which is embedded within the steel return yoke of the magnet. The inner tracking system consists of silicon pixel and strip detectors, and measures the trajectories of charged particles, and thus their curvature in magnetic field. Using this radius information, the ratio of transverse momentum to charge of the particle can be calculated. Each of the calorimeters are built from dense material designed to

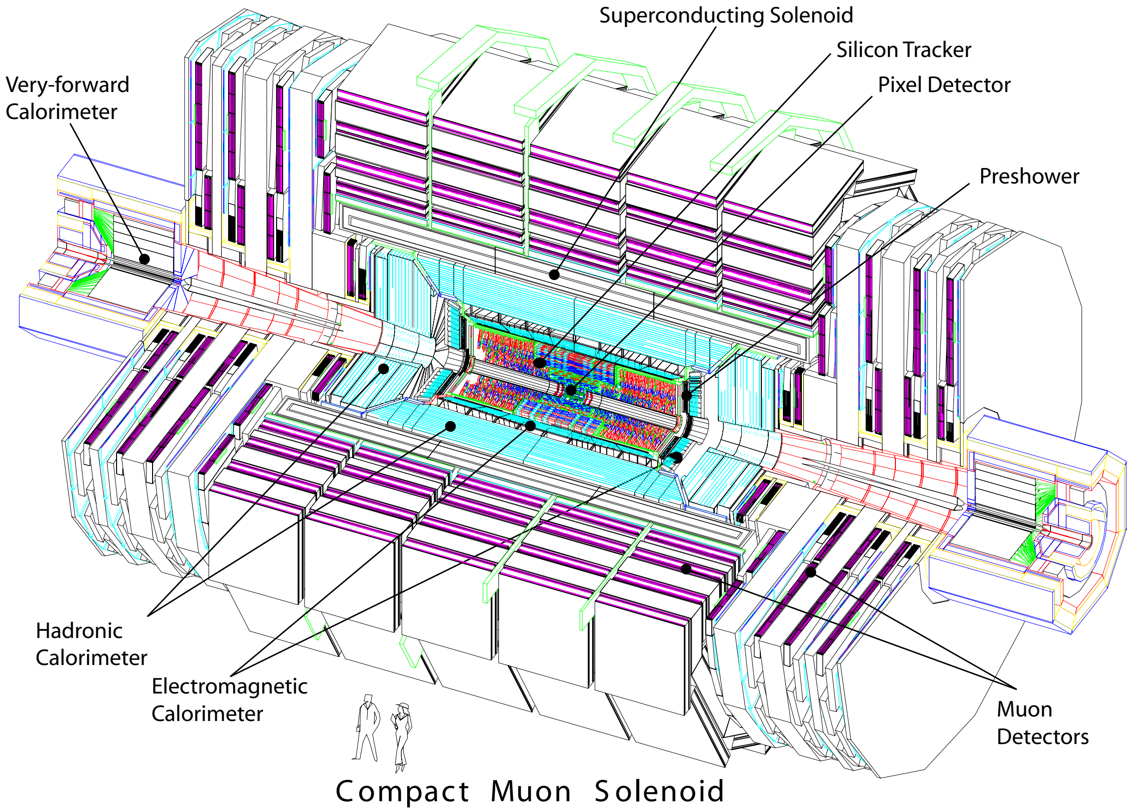

Figure 3.6: Component-labeled diagram of the CMS experiment [16]

cause electrons and photons in the ECAL, and hadrons in the HCAL in conjunction with the ECAL, to deposit all of their energy within the calorimeters. As the detector name suggests, a special muon system is also in place to measure the momentum and and position of minimum ionizing muons, or in this case, potential HSCPs. A depiction typical particle trajectories through the CMS modules is depicted in Fig. 3.7.

3.2.3 Inner Tracker

The inner tracker accomplishes two primary goals: the measurement of charged particle tracks along with their corresponding vertices (points of origin), as well as the measurement of the amount of energy deposited by a particle with the silicon detector [17]. Both of these capabilities are invaluable to the search for MCHSCPs, as well as to the general measurement and identification of electrons and muons.

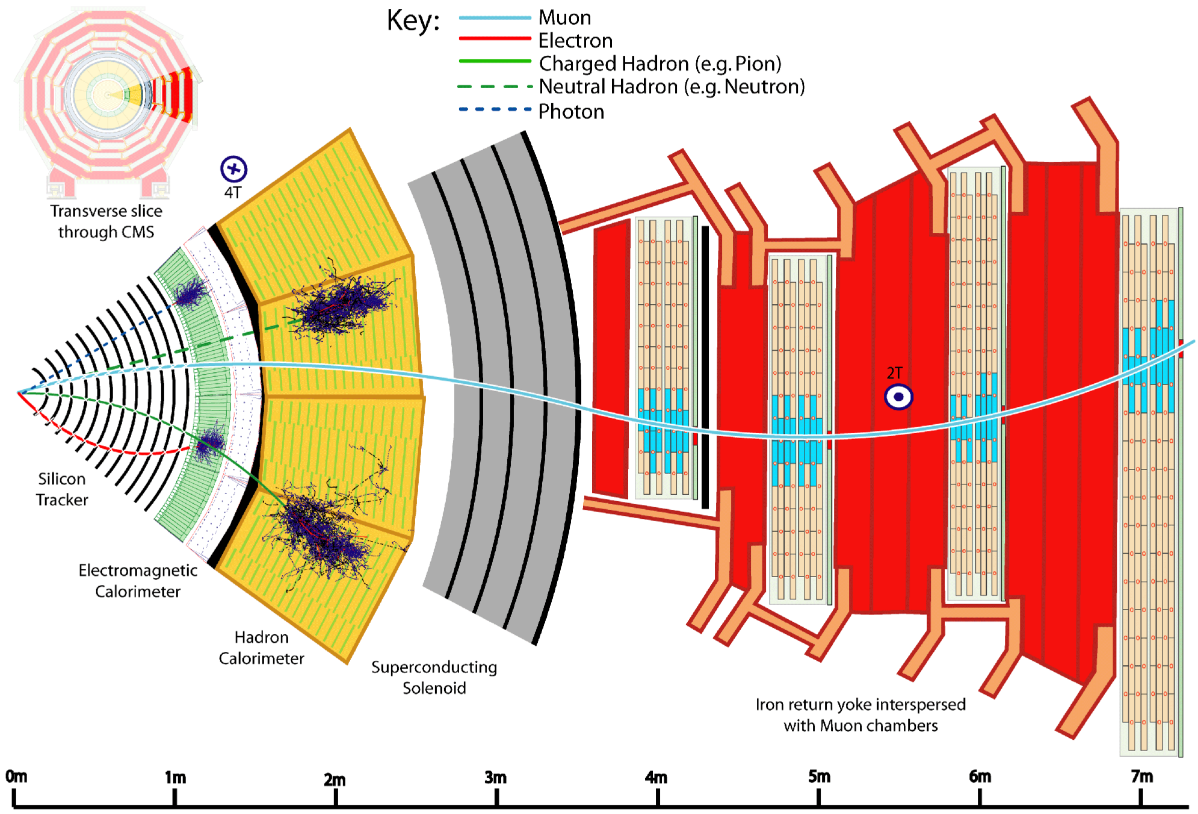

Figure 3.7: Transverse slice of the CMS detector with illustrated, typical charged particle propagation

The tracker is constructed entirely of silicon material due to its radiation tolerance, as well as its low atomic density which mitigates the scattering of the particles whose position it is tracking. The inner tracker consists of two systems: the pixel tracker located closest to the interaction point and the most granular of the two, and the strip tracker, which makes up the majority of the tracking system.

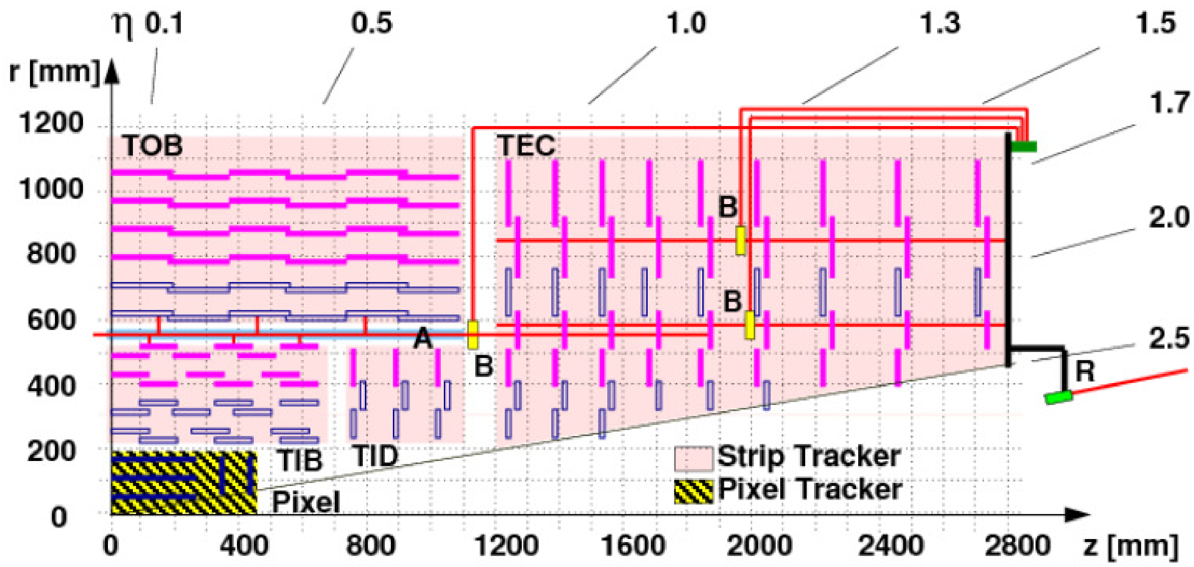

Figure 3.8: Schematic view of one quarter of the silicon tracker in the rz plane. The positions of the pixel modules are indicated within the hatched area. At larger radii within the lightly shaded areas, solid rectangles represent single strip modules, while hollow rectangles indicate pairs of strip modules mounted back-to-back with a relative stereo angle [18].

The strip tracker system is composed of silicon micro-strip detectors of varying size and shape, due to the inverse proportionality between particle flux and distance from the interaction point at the vertex. Hence, the strip area is increased with r. An alternative would be to simply use more strips of the same size as the radius is increased, but this would pose the problem of adding more readout channels. To mitigate this, strip length/area are increased as mentioned.

The system is composed of three sub-systems: the Tracker Inner Barrel (TIB) and Disks (TID), the Tracker Outer Barrel (TOB), and the Tracker EndCaps (TEC). In the barrel, a cylindrical layer of strip trackers is formed by placing individual strips parallel to the beam axis, giving $r\phi$ coverage. Likewise, the strips form a disk in the endcaps due to their radial placement, yielding coverage in $z\phi$. Thus, position measurements can be acquired through the exploitation of strip tracker information in $r\phi$ and $z\phi$.

In the search for HSCPs, the tracking system is also used to gather ionization energy loss information. As charged particles traverse the strip detector, they ionize the silicon, resulting in electron-hole pairs. Ideally, all of the ionization energy will be deposited in a single strip, or a single strip plus a direct neighbor. This, however, is not always the case. A constant electric field is used to collect the ionized charge, which is subsequently processed by readout electronics and converted into Analog to Digital Converter (ADC) counts. For a minimum ionizing particle, the energy loss corresponds to roughly $3\,\mathrm{MeV\,cm^{-1}}$, or in terms of counts, approximately 300 $\mathrm{ADCmm^{-1}}$. These counts are restricted to the dynamic range of roughly three times the energy deposition of a minimum ionizing particle, due to the 8-bit nature of the ADC. Theoretically, the ADC is capable of measurements in the range of 0 to 255 counts. Experimentally, noise in the strip detector dominates the energy range corresponding to ADC counts from 4 to 9, inclusively. A non-linear response of the ADC to deposited energy serves to further limit the effective, measurable range of energies [19]. The range is further limited on the high-end by the reservation of bits 254 and 255 for energy loss in the inclusive range of 254 to 1024 counts, and greater than 1024 counts, respectively. The combination of these limitations, although primarily the latter involving bits 254 and 255, are collectively referred to as the saturation effect [17].

The actual calculation of ionization energy deposited by a single particle involves combined information from multiple silicon strips. As aforementioned, an ideal scenario corresponds to a charged particle depositing the majority of its energy in a single strip, or two neighboring strips. Offline (post-data taking) reconstruction necessitates the creation of strip clusters, using those strips with a signal to noise ratio greater than 3 as seeds. Once a seed has been selected, neighboring strips are serially searched for signal to noise ratios greater than 2. If this is true, the strip is included in the cluster.

Energy deposited in the seed strips will likely be shared with the neighboring strips. Experimentally, it has been shown that further sharing can occur with a factor of 10^{-n} to neighboring strips, where $n = 1$ is the seed strip direct neighbor [20]. There exist restrictions on clusters even after they are created, as noise fluctuations in strips could mimic a viable HSCP, or even SM signature. The primary restriction dictates that the total signal size of the cluster must be larger than 5 times the square root of the sum of the Root Mean Squared (RMS) noise, squared, of its constituent silicon strips. Once a strip cluster passes all of the necessary prerequisites, information regarding the particle that nominally created it may be acquired. The cluster charge is calculated as the un-weighted sum of the charges in the individual strips making up the cluster. The total energy loss, $\frac{\Delta E}{\Delta x}$ is defined as the charge deposited per unit path length, and is therefore calculated by dividing the cluster charge (ΔE) by the geometric path length (Δx). Δx is defined by $\Delta x \equiv L/\cos\theta$, where L is the module thickness, and θ the angle between the track of interest and the normal to the strip module of interest [20].

3.2.4 Electromagnetic Calorimeter

The CMS ECAL is a hermetic and homogeneous, crystal-based scintillating calorimeter, whose primary function is the accurate energy measurement of electromagnetic particles (i.e. electrons and photons). Its hermeticity is characterized by its constituent barrel (EB) and two sealing endcaps (EE). The ECAL contains 61200 $PbWO_4$ scintillating crystals mounted in the EB, with each EE containing 7324 crystals [11]. The choice of $PbWO_4$ ensures the compactness of the detector with a radiation length of approximately 0.85 cm, and Moliere radius on the order of 2.19 cm, which further ensures the radiation hardness necessary to cope with the harsh environment at the LHC [21]. Pseudorapidity coverage in the ECAL extends to $|\eta| < 2.5$. In conjunction with the silicon tracker (Sec. 3.2.3) and solenoid magnet (Sec. 3.2.2), the ECAL is used to reconstruct the momentum of charged particles, especially electrons and photons to which it exhibits the highest sensitivity

[21].

3.2.5 Hadronic Calorimeter

The main function of the HCAL is, as its name implies, to accurately measure the energy and direction of hadrons (Sec. 2.2) [22]. The HCAL is a sampling calorimeter consisting of alternating layers of brass and/or steel absorber, and plastic scintillator. Geometrically, it has a much larger pseudorapidity coverage ($|\eta| < 5.3$) than does the ECAL that it surrounds.

Like the ECAL, the HCAL consists of a barrel (HB) and endcap (HE). In addition to these, the HCAL also contains outer (HO) and forward (HF) components, which in conjunction with the ECAL further increase the hermeticity of the detector as a whole. Unlike the ECAL which generally stops electromagnetic particles within its confines, it is not uncommon for hadrons to breach the HCAL. As such, the solenoid itself is also used as an absorber, along with the outer HCAL segment which is placed just outside of it.

3.2.6 Muon System

Although the muon system is not surrounded by the solenoid as the tracker, ECAL, and HCAL are, the magnetic field is still channeled through it and retained by the usage of iron plates. As such, the momentum of muons and/or HSCPs can be measured in both the solenoid as well as the muon system. This is imperative, as similar to muons, HSCPs are minimal ionizing and will likely not be stopped within the ECAL or HCAL. While the momentum signatures of HSCPs and muons are not necessarily readily distinguishable, their time of flight signatures are, and it is by making this measurement possible that the muon system serves as a crucial piece of this investigation [23].

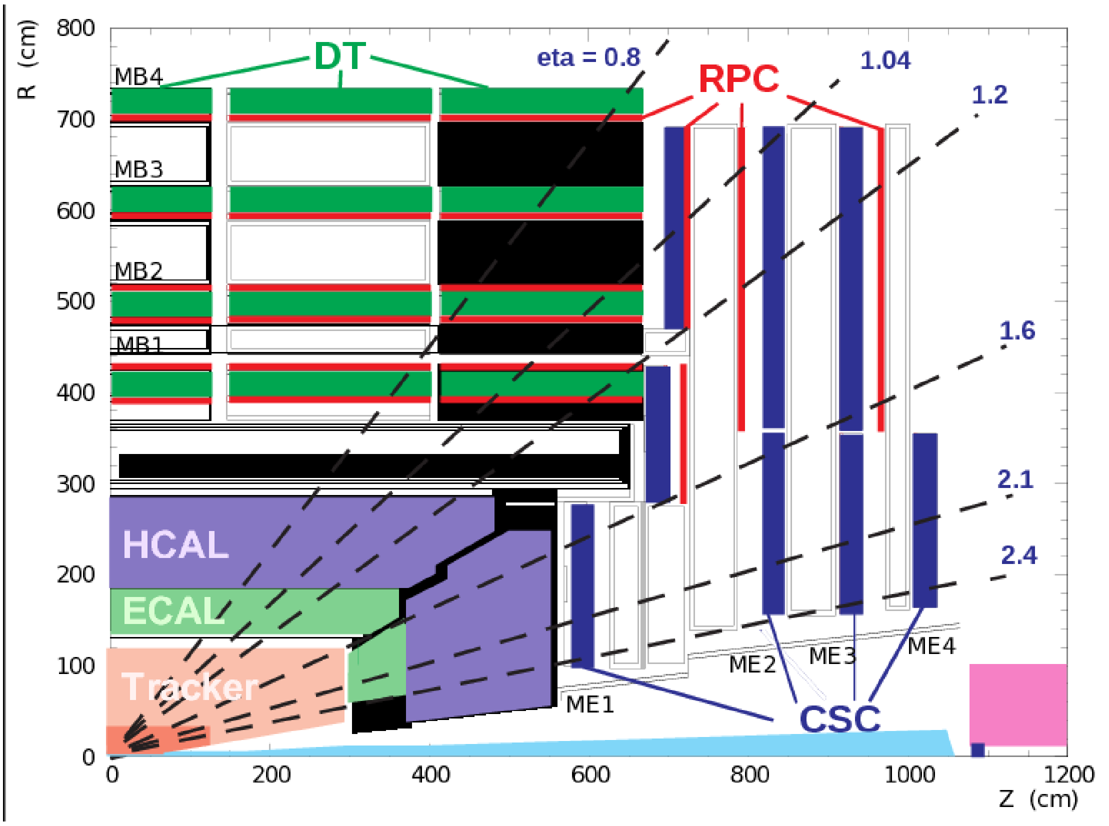

Figure 3.9: Longitudinal layout of one quadrant of the CMS detector. The four DT stations in the barrel (MB1–MB4, green), the four CSC stations in the endcap (ME1–ME4, blue), and the RPC stations (red) are shown [24].

The muon system records both arrival time and position information for traversing particles. Muons will be traveling at roughly the speed of light, c, whereas HSCPs can be expected to have significantly lower speed (and therefore later arrival times) compared to muons. Thus, time of flight information can be exploited as a means of identifying HSCP candidates. As depicted in Fig. 3.9, the muon system is comprised of three gaseous detector components: Drift Tube chambers (DT), Cathode Strip Chambers (CSC), and Resistive Plate Chambers (RPC) [23]. While the RPC and CSC are important to the CMS experiment as a whole, this analysis relies most heavily on the DT.

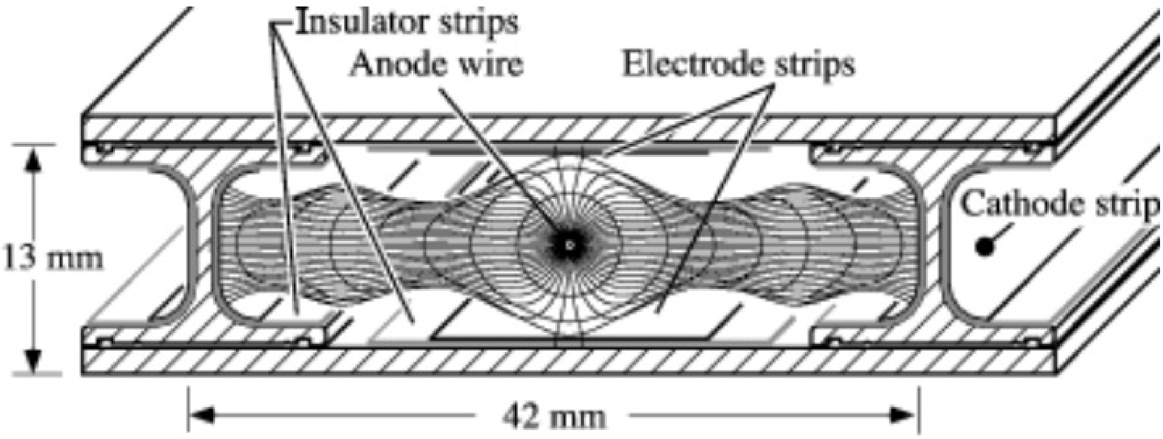

Figure 3.10: Layout of a DT cell, showing the electric field lines in the gas volume [15]

The drift tube system is located within the barrel of the detector, where muon rates are low, and the return magnetic field is relatively uniform and weak[23]. Each tube is 4 cm wide, and contains a stretched wire within a gaseous volume. A schematic cross section of a DT is depicted in Fig. 3.10. To avoid edge-effects and enable the determination of the particle path relative to the central wire, DTs are staggered by half of their size.

As charged particles pass through the gaseous volume, they ionize the contained gas, knocking electrons off of these atoms. These electrons are accelerated by an electric field (Fig. 3.10) to the positively charged wire within the tube. Two-dimensional position reconstruction is made possible by combining signal amplitudes from multiple tube wires. Further, timing information can be obtained if one knows the average drift velocity of electrons in the gas. Thus, both trajectory and time of flight measurements may be made within the muon system.

4 Search Variables

The multiply charged analysis utilizes ionization energy deposition and time of flight information to search for HSCP candidates. These candidates are distinguished from typical SM signals through a calculated discriminator.

Note: The following sections display plots with cluster cleaning and cross-talk measures being turned on and off. For a description of these processes, refer to Sec. 5.2.1 and Sec. 5.2.2, respectively.

4.1 Momentum

Particle reconstruction in the CMS experiment is conducted under the assumption that all particles are singly charged ($|Q| = 1e$). Reconstructed momentum is calculated based on the curvature of a particle track of electric charge q within a homogeneous magnetic field as follows:

$$\begin{aligned} \vec{F}_{EM} &= q(\vec{E} + \vec{v} \times \vec{B}) \\ &= qvB \sin\theta \\ \vec{F}_{EM} &= qvB \end{aligned} \tag{4.1}$$

where $\vec{F}_{EM}$ represents the total electromagnetic force acting on the particle, $\vec{E}$ represents the electric field which is zero in the region of momentum measurement, $\vec{B}$ represents the magnetic field, and $\vec{v}$ represents the velocity of the particle. The motion the particle is helical in nature. With the magnetic force from Eq. 4.1 acting as a centripetal force we have that

$$\begin{aligned} qvB &= (mv)\left(vr^{-1}\right) \\ qB &= pr^{-1} \\ p &= qBr \end{aligned} \tag{4.2}$$

where p represents the magnitude of the reconstructed track momentum. Eq. 4.2 shows a linear dependence of the reconstructed momentum magnitude p on both the charge of the particle and the radius of its trajectory. Multiply charged particles will therefore have their momentum misreconstructed by a factor of inverse charge. This is demonstrated in Eq. 4.3 by taking the ratio between reconstructed momentum assuming a unity elementary charge, e, and a mHSCP with charge of some integer, α, times e. Figure 4.1(a) displays reconstructed particle momentum as a function of generated particle momentum for varying particle charges. The distributions of the momenta ratios agree with the plotted inverse charge lines.

$$\begin{aligned} \frac{p_r}{p_g} &= \frac{eBr}{\alpha eBr} \\ \frac{p_r}{p_g} &= \frac{1}{\alpha} \\ p_r &= \frac{p_g}{\alpha} \end{aligned} \tag{4.3}$$

Correcting the reconstructed momenta (p_r) by multiplying by the respective α (Eq. 4.3) yields Fig. 4.1(b), where the correction indeed results in a 1:1 correspondence between generated (p_g) and reconstructed momenta.

Figures 4.2 and 4.3 display a shift in transverse momentum distributions with increasing

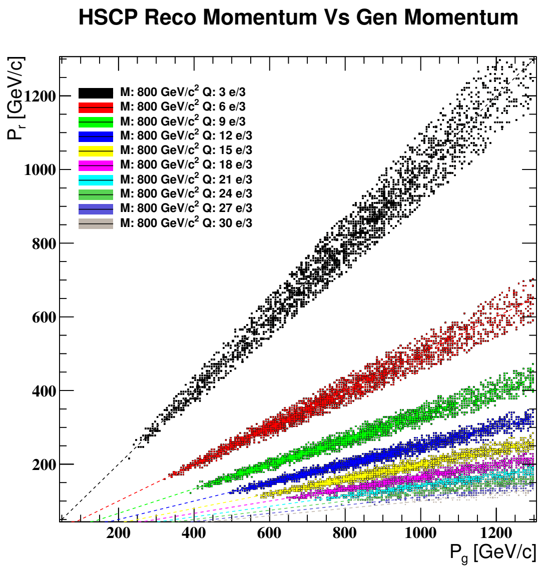

(a) Unscaled

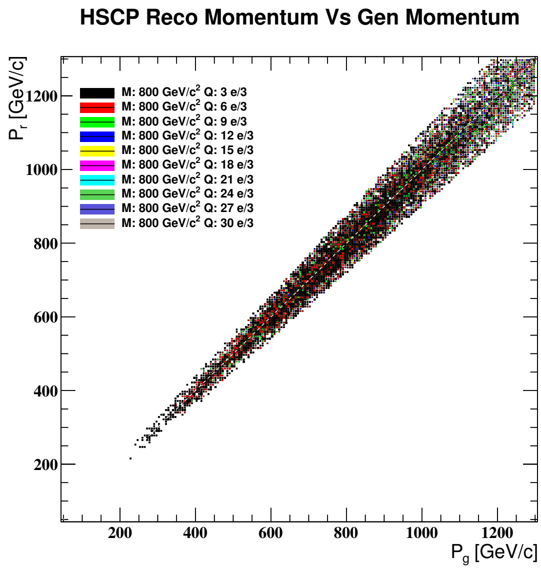

(b) Scaled

Figure 4.1: Distributions of reconstructed momentum versus generated momentum for $\sqrt{s}$ = 13 TeV simulated mHSCPs. Unaltered reconstructed momenta are displayed in plot (a), while scaling by a factor of α (Eq. 4.3) is performed in plot (b).

mass for HSCPs, as well as a shift pseudorapidity towards the central region ($\eta = 0$).

4.2 Pseudorapidity

As the mass of interacting particles increases, the reconstructed η distribution shifts toward the central region. This corresponds to a larger polar angle, θ, and therefore a reaction plane tending towards orthogonality with the beam axis. Figure 4.4 displays this trend, with the reconstructed mHSCP η distributions tending towards the central region as the particle mass increases. The discrepancy between the SM simulation and experimental observation stems from the fact that there are processes that occur that are not included in the simulation, which is limited to Drell-Yan$\rightarrow$ $\mu\mu$ processes.

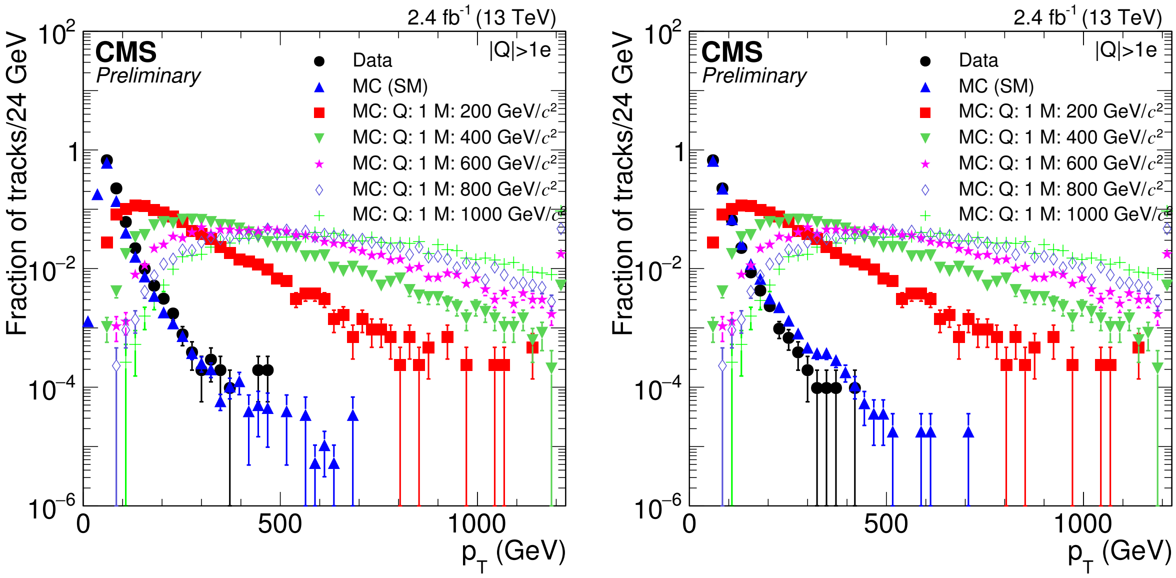

(a) CC CT (b) None

Figure 4.2: Distributions of reconstructed transverse momentum for $\sqrt{s} = 13$ TeV simulated mHSCPs and SM, as well as data. Plot (a) displays data and simulation with cluster cleaning and cross talk inversion both turned on, while plot (b) shows the same data and simulation with cleaning and inversion turned off.

4.3 Discriminator

In order to distinguish HSCP signal from typical SM background, it is desirable to have a mathematical construct that is sensitive to particles with ionization significantly greater than that of a minimally ionizing particle. Further, it will be useful for this measure to overcome the effects of saturation described in Sec. 3.2.3. The primary discriminator used in this investigation is the Asymmetric Smirnov-Cramer-von Mises (I_{as}), which is a custom extension of the Smirnov-Cramer-von Mises discriminator made to be more sensitive to higher-than-MIP ionization [3][4][25]. Essentially, any discriminator seeks to measure the difference between an empirical and observed probability distribution function (PDF). In the case of the HSCP search, the PDF of a minimum ionizing particle (MIP) is assumed to be known. Specifically for this search, the discriminator seeks to measure compatibility between a set of $\Delta E/\Delta x$ measurements and the MIP PDF. I_{as} is designed to be sensitive to incompatibility with the MIP hypothesis for extremely large ionizations, i.e. the characteristic regime of parameter space for a mHSCP characterized

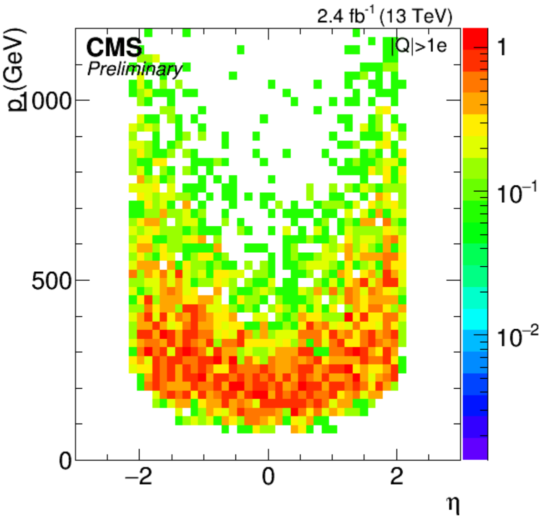

(a) 200 GeV

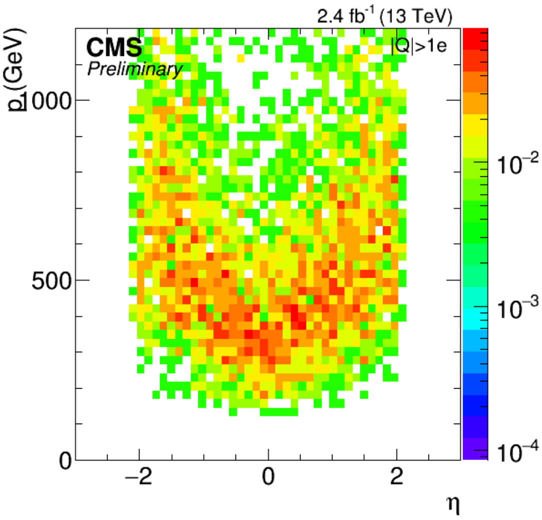

(b) 400GeV

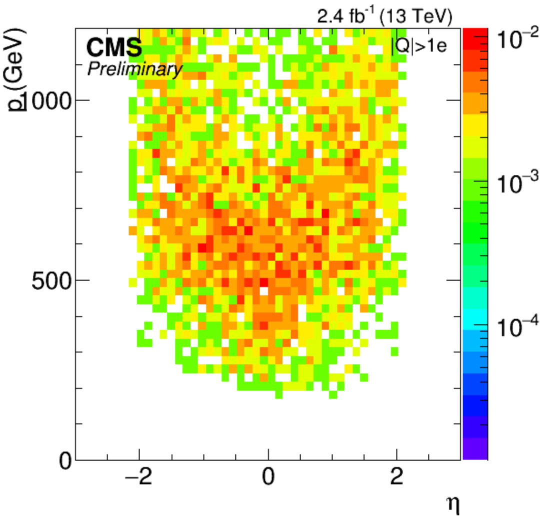

(c) 600 GeV

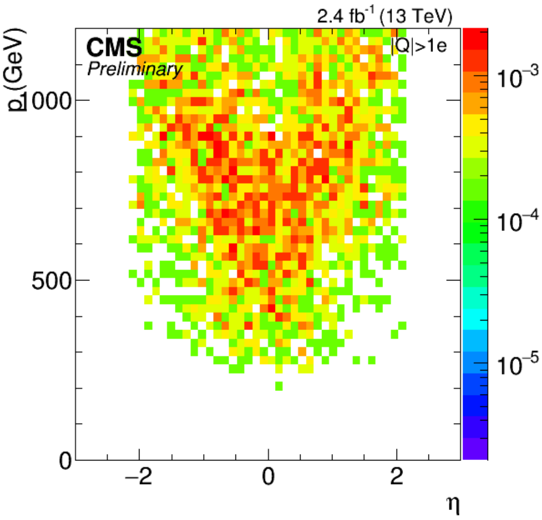

(d) 800GeV

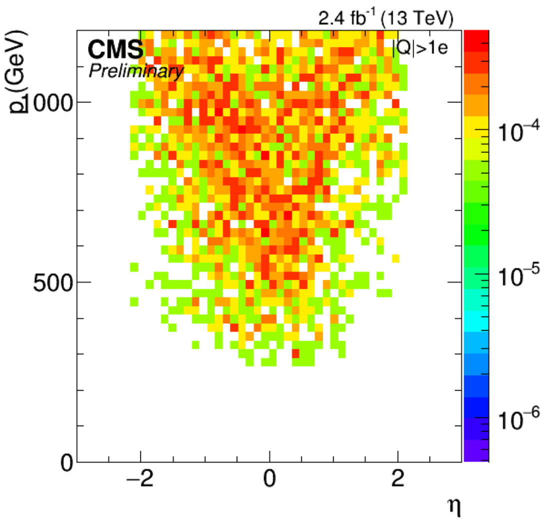

(e) 1000 GeV

Figure 4.3: Distributions of reconstructed momentum vs pseudorapidity with both cluster cleaning and cross talk inversion turned on from $\sqrt{s} = 13$ TeV mHSCP simulation . Masses of 200 (a), 400 (b), 600 (c), 800 (d), and 1000 (e) GeV are displayed.

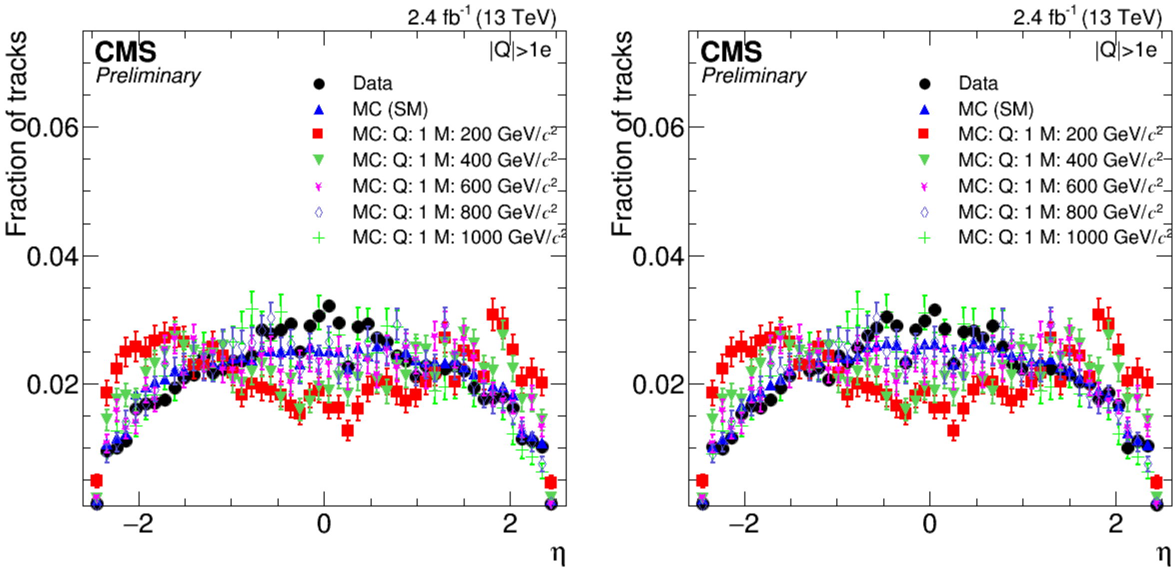

(a) CC CT

(b) None

Figure 4.4: Distributions of reconstructed pseudorapidity for $\sqrt{s} = 13$ TeV mHSCP and SM simulation, as well as data. Left (a) has both cluster cleaning and cross-talk inversion turned on, while right (b) has both turned off.

by high mass or charge. If a candidate track is compatible with the MIP hypothesis, it will have an I_{as} close to zero. Similarly, a candidate track with greater ionization will have an I_{as} closer to one. Figure 4.5 display increasing I_{as} as a function of mass for mHSCP simulation. Each mass exhibits higher values of I_{as} associated with lower values of momentum, signifying increased ionization. These stand in stark contrast with the data and SM simulation displayed in Fig. 4.6, each of which is characterized by both low momenta and low calculated discriminator values, signifying minimum ionization.

The formula for the discriminator is given by

$$I_{as} = \frac{3}{N} \times \left(\frac{1}{12N} + \sum_{i=1}^{N} \left[P_i \times \left(P_i - \frac{2i-1}{2N} \right)^2 \right] \right)$$

where N is the number of dE/dx measurements taken, and P_i is the probability for the i^{th} measurement that a MIP would have the same or a lesser $\Delta E/\Delta x$. Figure 4.7 shows the sensitivity of the discriminator to high mass, elementary charged particles. The Standard Model simulation and data have low ($I_{as} < 0.4$) values of the discriminator,

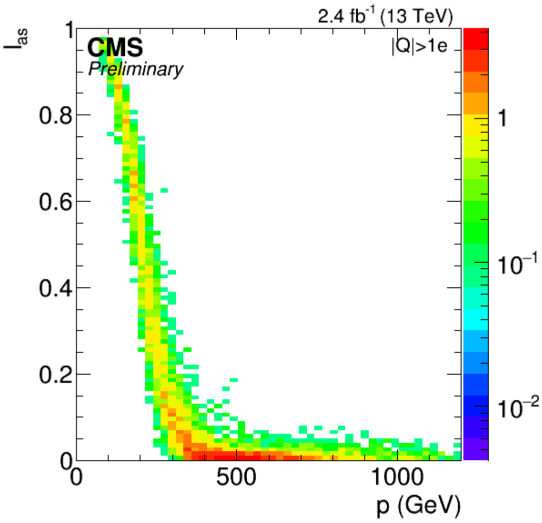

(a) 200 GeV

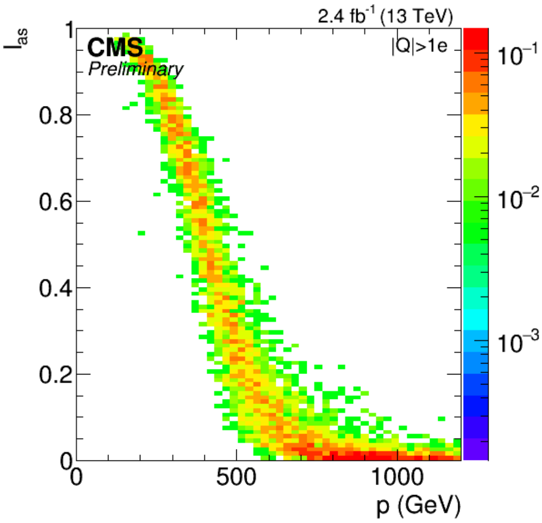

(b) 400GeV

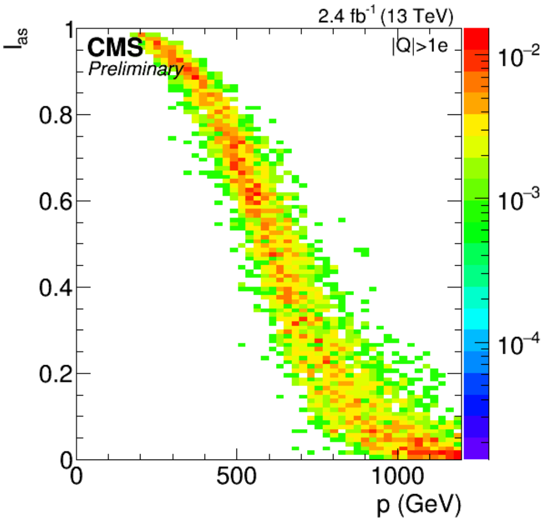

(c) 600 GeV

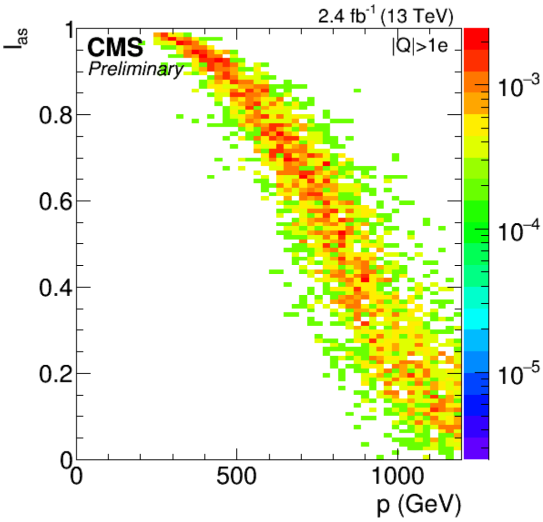

(d) 800GeV

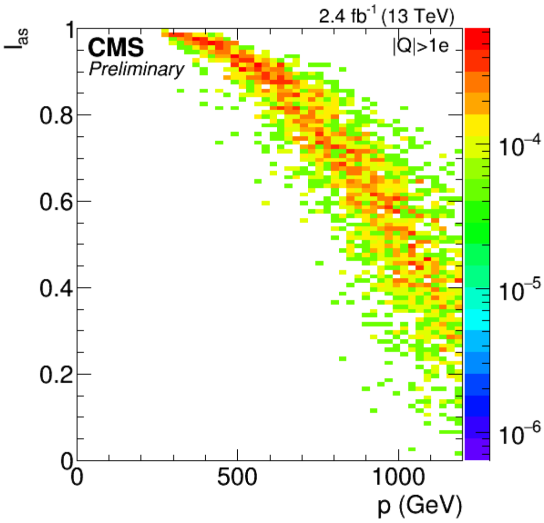

(e) 1000 GeV

Figure 4.5: Distributions of calculated discriminator vs reconstructed momentum for $\sqrt{s}$ = 13 TeV mHSCP simulation and data with both cluster cleaning and cross-talk inversion turned on. Masses of 200 (a), 400 (b), 600 (c), 800 (d), and 1000 (e) GeV are displayed.

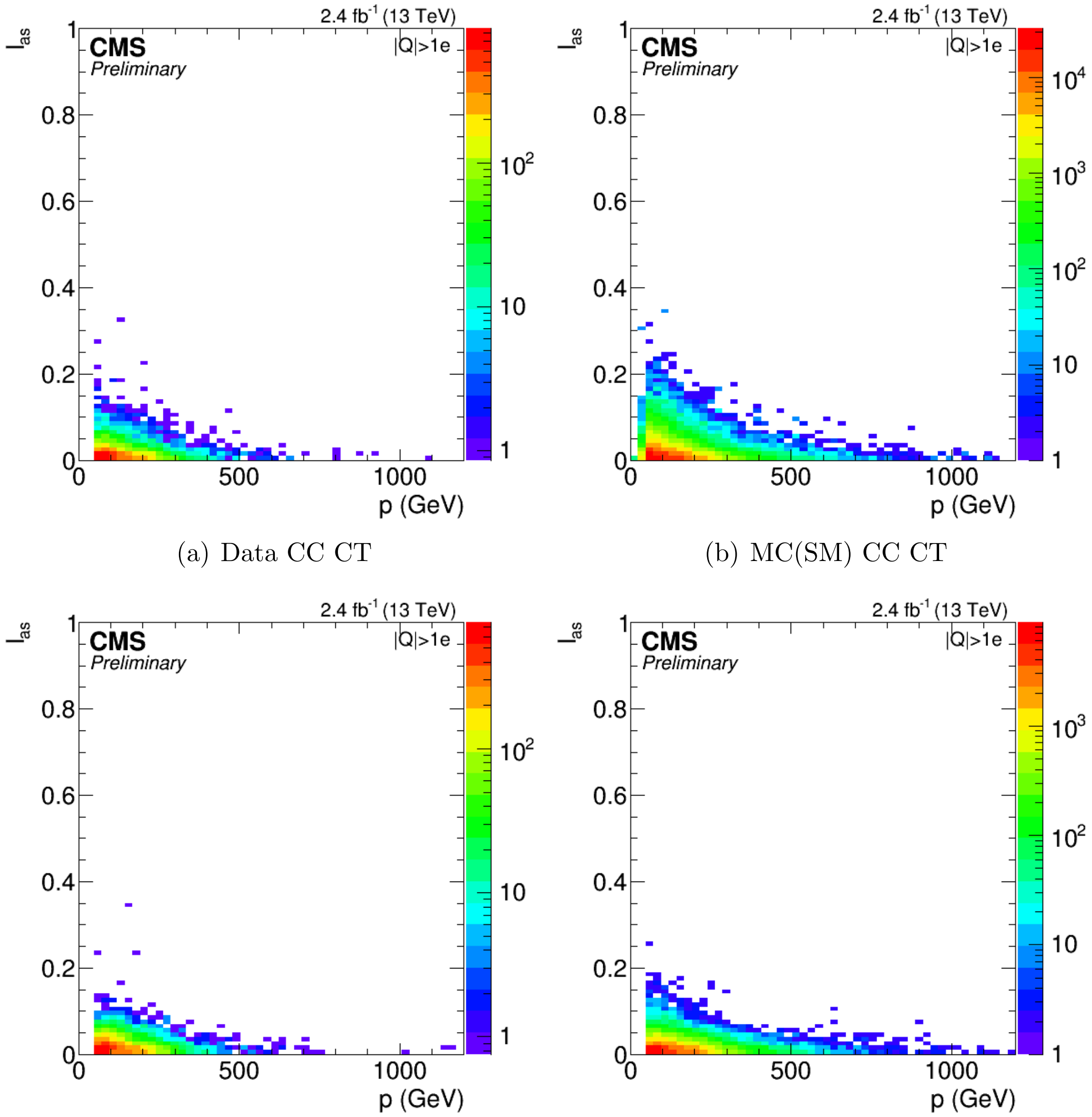

(a) Data CC CT

(b) MC(SM) CC CT

(c) Data None

(d) MC(SM) None

Figure 4.6: Distributions of discriminator versus reconstructed momentum for $\sqrt{s} = 13$ TeV data and SM simulation with cleaning and inversion turned on (a,b) and off (c,d).

whereas the mHSCP simulation exhibits discriminator values ranging up to 1, signifying incompatibility with the MIP hypothesis.

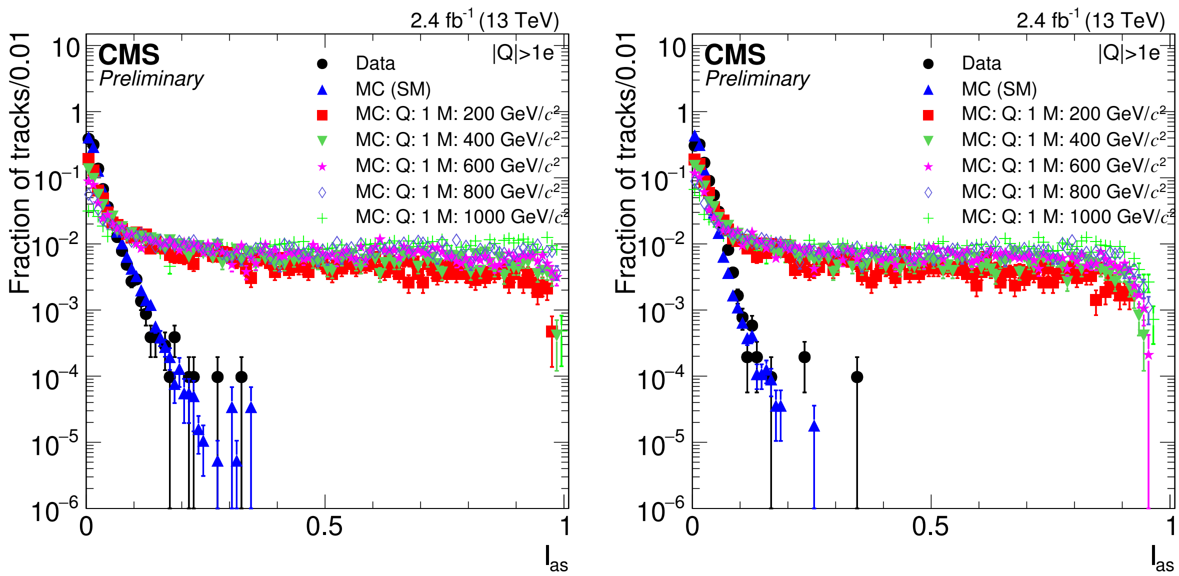

(a) CC CT

(b) None

Figure 4.7: Distributions of calculated I_{as} for $\sqrt{s} = 13$ TeV mHSCP and SM Simulation. Left (a) has both cluster cleaning and cross-talk turned on, while right (b) has both turned off.

4.4 Ionization Energy Deposition

mHSCPs will experience increased ionization energy loss due to their increased charges. The mean rate of energy loss by moderately relativistic charged heavy particles is governed by the Bethe-Bloch equation [28]

$$-\left\langle \frac{dE}{dx} \right\rangle = 4\pi N_A r_e^2 m_e c^2 z^2 \frac{Z}{A}\frac{1}{\beta^2}\left[\frac{1}{2}\ln\frac{2m_e c^2\beta^2\gamma^2 T_{max}}{I^2} - \beta^2 - \frac{\delta(\beta\gamma)}{2}\right] \times Q^2 \qquad (4.4)$$

where N_a is Avogadro's number, r_e is the classical electron radius, m_e is the mass of the electron, c is the speed of light vacuum, z is the electric charge of the particle (in e/3), Z is the absorber atomic number, A is the absorber mass number, β is the ratio of particle speed to the speed of light (c), γ is the Lorentz factor $\gamma = \frac{1}{\sqrt{1-\beta^2}}$, T_{max} is the maximum kinetic energy that can be imparted on a free electron in a single collision, I is the mean

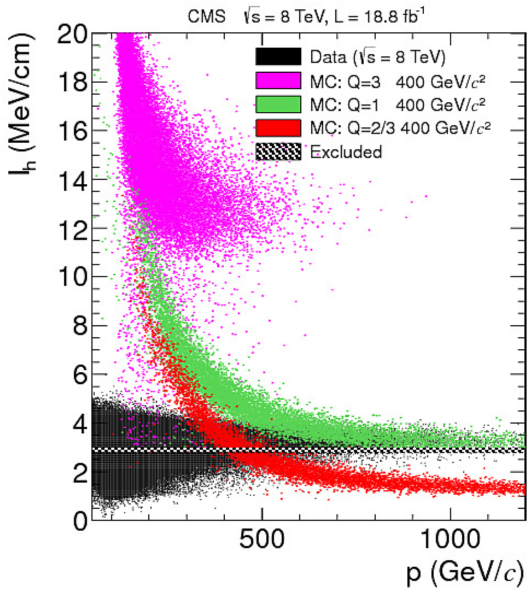

(a) Data 7 & 8 TeV

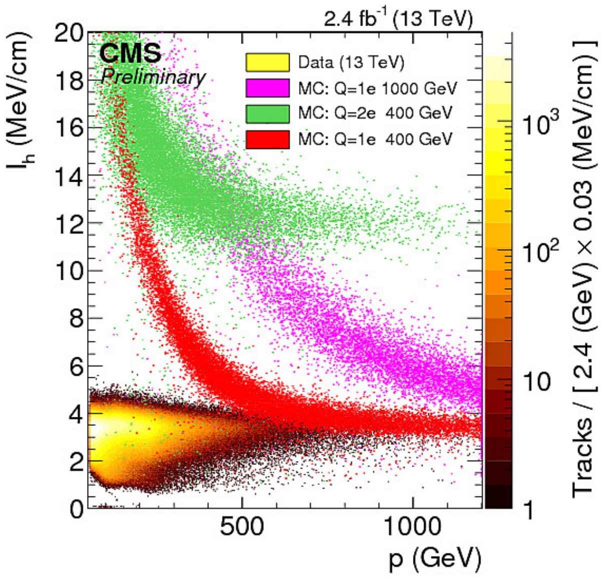

(b) Data 13TeV

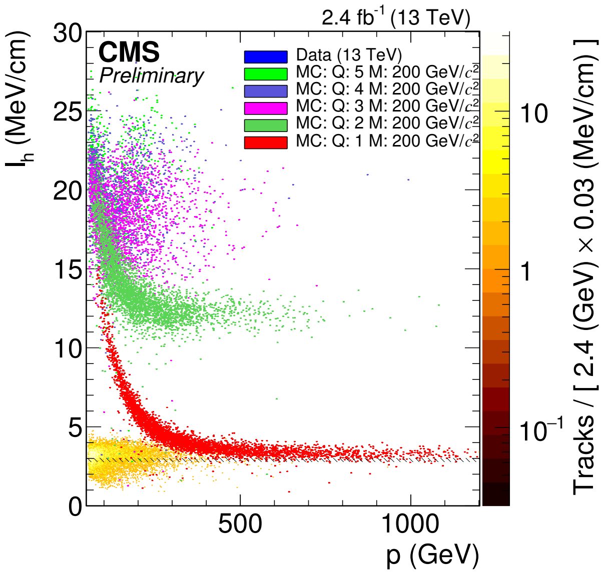

(c) 13 TeV CC CT

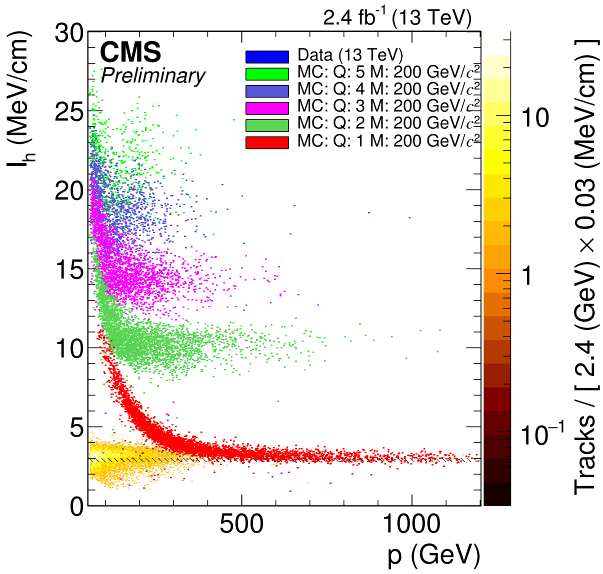

(d) 13 TeV None

Figure 4.8: Distributions of dE/dx estimator (I_h) versus momentum for the 2012, 8 TeV data (a), with singly and fractionally charged simulation; 2015, 13 TeV data (b), with singly and multiply charged simulation [26][27], and 13 TeV data with mHSCP simulation with (c) and without (d) cluster cleaning and cross-talk inversion turned on.

excitation potential, $\delta(\beta\gamma)$ is Fermi's density correction, and Q is the electric charge of the particle. In general, ionization energy loss of a charged particle in a material can be qualitatively described by the following: energy loss reaches a minimum at relativistic speed ($\beta\gamma \simeq 2$), and beyond this energy loss is roughly constant until radiation effects dominate. For non-relativistic speeds ($0.1 < \beta\gamma < 2$), the energy loss is proportional to $\frac{1}{\beta^2}$. Finally, there is an overall Q^2 dependence on the charge of the particle, displayed by the formation of and separation between visible bands in Fig. 4.8.

Due to the highly probabilistic nature of ionization energy deposition, large fluctuations in individual $\Delta E/\Delta x$ measurements are observed [5]. Specifically, the fluctuations follow a Landau distribution for charged particles in a thin medium [28]. As such, it is necessary to utilize an estimator that describes the most probable energy loss for the track of interest, based on all of the individual $\Delta E/\Delta x$ measurements obtained. The estimator of choice for this investigation is known as the harmonic mean, I_h. Qualitatively, the harmonic mean is defined as the number of terms divided by the sum of the terms' reciprocals [19]. Mathematically, I_h is defined by

$$I_h = \left(\frac{1}{N} \sum_{i=1}^{N} \left(\frac{\Delta E}{\Delta x} \right)_i^k \right)^{\frac{1}{k}} \tag{4.5}$$

where specifically, the squared harmonic mean ($k = -2$) has been utilized due to its useful property of suppressing higher individual IE values. As such, a typical SM particle with a few randomly high IE fluctuations will be readily distinguishable from a true HSCP or mHSCP, both of which would be characterized by several large individual IE measurements. Figure 4.9 corroborates this claim by displaying a far larger fraction of HSCP tracks with higher I_h as compared to SM simulation and data.

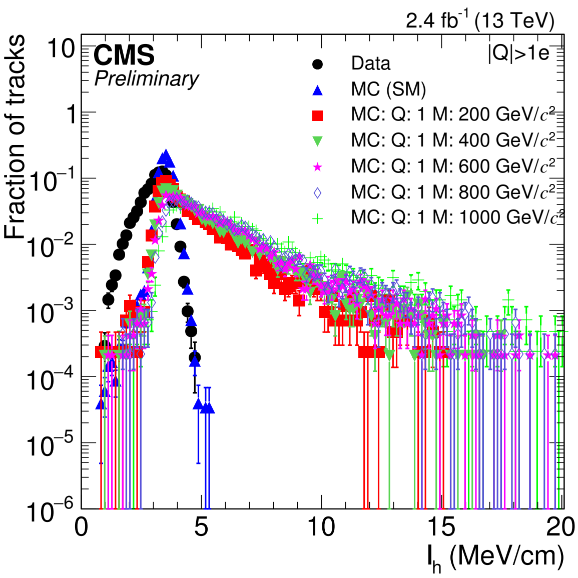

(a) CC CT

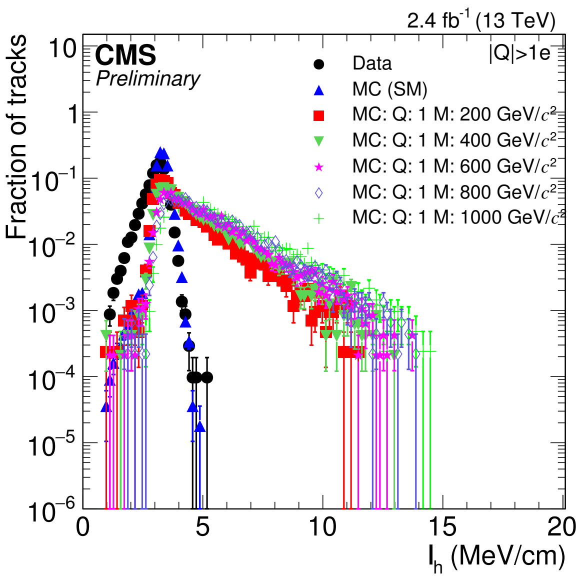

(b) None

Figure 4.9: Distributions of estimated ionization (I_h) for $\sqrt{s}$ = 13 TeV mHSCP and SM simulation, and data. Left (a) has both cluster cleaning and cross-talk inversion turned on, while right (b) has both turned off.

4.5 Time of Flight

Due to their increased mass, HSCPs and mHSCPs will, for a given momentum, tend to move slower than typical SM particles ($\beta \simeq 1$). Thus, time-of-flight information can be used to identify potential HSCP candidates. As described in Sec. 3.2.6, drift tubes in the muon system are used to calculate TOF information based on the known propagation times of electrons within the ionized gas of the tubes.

4.5.1 Drift Tube Time Measurements

As charged particles traverse the DTs, the gas within the tubes becomes ionized. Due to an electric field between the anode and cathode within the tube, electrons are accelerated towards the central anode wire, transmitting amplitude and time information to readout instrumentation. The time of flight calculation therefore depends on four independent timing measurements: the time of flight of a SM charged particle from the interaction point to the muon system (t_c), the drift time of the electrons in the tubes (known from muon calibration [24]), the propagation time of the signal along the central wire (t_w), and an off-time correction for delayed particles (δt) (Sec. 3.2.6).

Due to the staggered placement of the drift tubes, initial timing information from t_w and t_c can be used to reconstruct a preliminary trajectory in two dimensions for an assumed SM particle. Different values of δt are then iterated over until the timing measurements in the DT cells have been matched. A positive value of δt has the effect of shifting the reconstructed particle trajectory towards the central wire of the cell in question, whereas negative values will shift it towards the edge. Once the best δt value has been determined, it can be used to calculate the inverse β (time of flight) of the traversing particle.

4.5.2 Inverse β

The δt quantity is equal to the difference in travel time to the drift tube between a particle with speed βc, and a SM particle traveling at approximately the speed of light, c. Letting L be the distance from the interaction point to the muon system, and noting that travel time is equal to the distance traveled divided by the speed we have that

$$\delta t = \frac{L}{\beta c} - \frac{L}{c} \tag{4.6}$$

and rearranging to solve for inverse β we get

$$\frac{1}{\beta} = 1 + \frac{c\delta t}{L} \tag{4.7}$$

where now, an inverse β measurement can be taken in each individual drift tube, and an average value calculated. A weighted average is used, with the weight for the i^{th} drift tube given by

$$w_i = \frac{(n-2)}{n} \frac{L_i^2}{\sigma_{DT}^2} \tag{4.8}$$

where n is the number of measurements in the DT chamber used to constrain δt and $\sigma_{DT} = 3\,\text{ns}$ is the DT time resolution. The $\frac{n-2}{n}$ factor accounts for the fact that the δt values are calculated using two parameters of a straight line, determined from the same n measurements. In general, average time of flight and therefore inverse β will increase with particle mass. This is evidenced by Fig. 4.10. Further, the HSCP simulation exhibits larger TOF values than do either the SM simulation or the data.

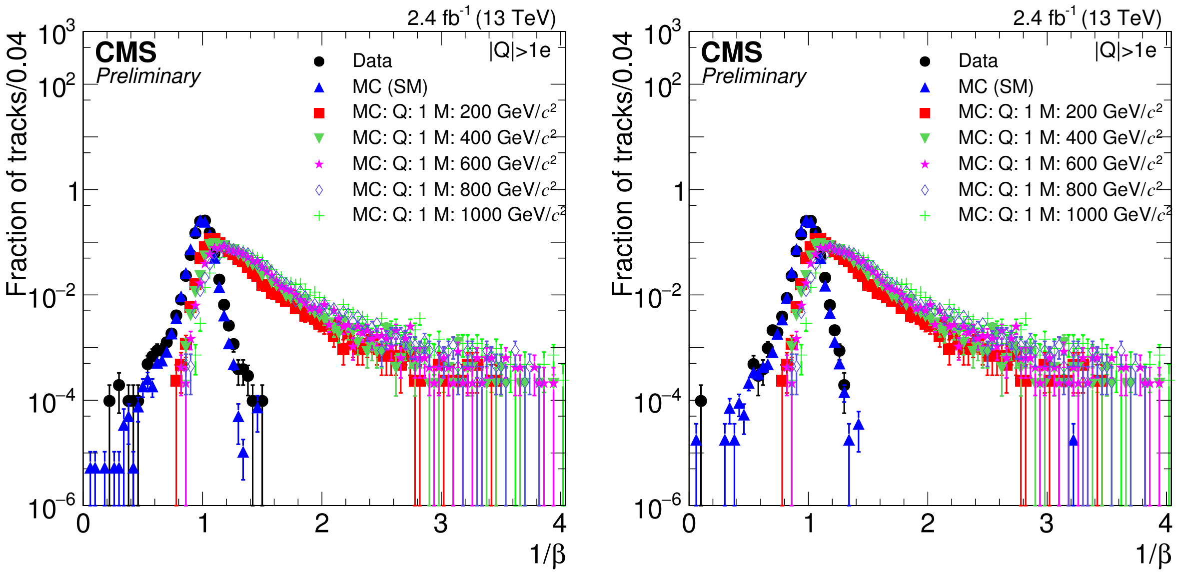

(a) CC CT

(b) None

Figure 4.10: Distributions of calculated time of flight $(\frac{1}{\beta})$ for $\sqrt{s} = 13$ TeV mHSCP and SM simulation, and data. The left plot (a) has both cluster cleaning and cross-talk inversion turned on, while the right plot (b) has both turned off.

5 Multiply Charged HSCP Analysis

The multiply charged HSCP analysis searches for mHSCPs that are observed in both the tracker and the muon system. Slow moving and highly ionizing particles are identified based on time of flight measurements in the muon system as well as ionization energy loss in the inner tracker. Stable, multi-charged supersymmetric tau particles were created using PYTHIA version 6 [29]. The propagation of the signal samples through the CMS detector systems was simulated using the GEANT4 framework [30]. Information on the behavior of the simulated particles is given in Chapter 4.

Online selection criteria describing missing transverse energy and efficiency triggers can be viewed in Ref. [3].

5.1 Data Selection

The analysis relies on $\frac{dE}{dx}$ and time of flight measurements from the tracker and muon systems, respectively. The first offline selection criterion involves matching a reconstructed track within the tracker system to one in the muon system. The resulting match is known as a global muon. The global muon track must have no fewer than six $\frac{dE}{dx}$ measurements in the strip detector in order to ensure reliable calculation of $\left\langle \frac{dE}{dx} \right\rangle$, with the number of measurements being equal to the number of strip and pixel measurements minus the

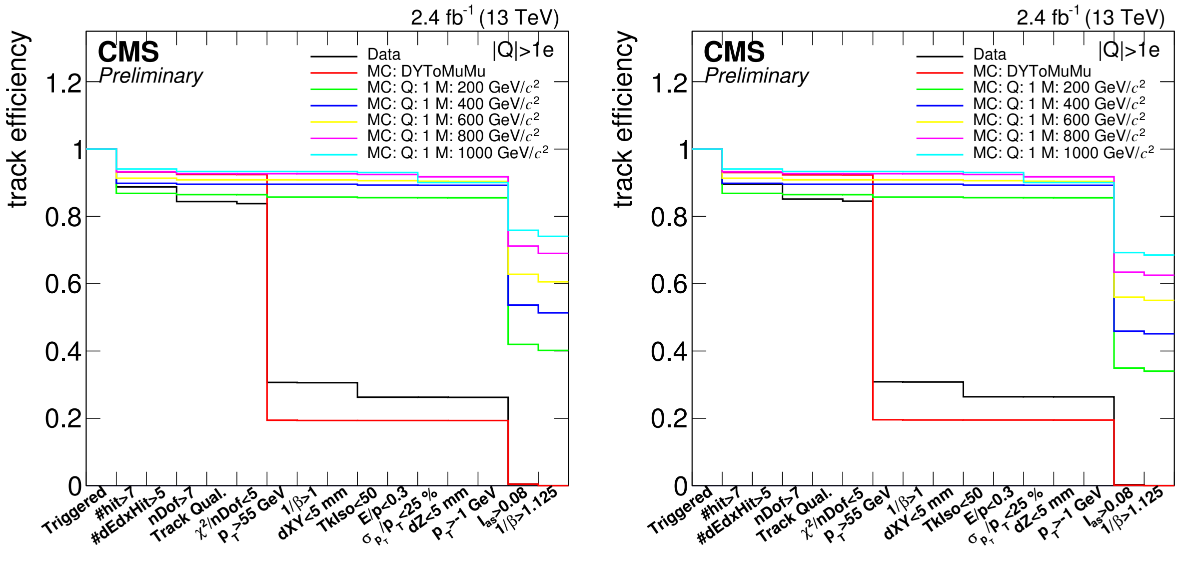

(a) CC CT

(b) None

Figure 5.1: Effects of various offline selection criteria applied to 13 TeV data and SM simulation, as well as mHSCP simulation with cluster cleaning and cross-talk applied in the left plot (a) and absent in the right plot (b).

number of cluster cleaned measurements. Similarly, at least 8 time of flight measurements must be made in the muon system layers with a minimum of 6 existing exclusively in either the DTs or CSCs in order to ensure a reliable estimate of $\langle 1/\beta \rangle$. This average must be greater than 1.075, signifying a non-relativistic particle. Further, the uncertainty on $\langle 1/\beta \rangle$ must be below 15%. To maximize the reliability of a global muon track fit, quality and χ^2/NDF requirements are also applied. A quality requirement of greater than 1 is imparted on all candidates, with a quality of 2 representing a perfectly "pure" track. A χ^2/NDF limit of no more than five as well as a relative error cut on the transverse momentum measurements (σ_{p_t}/p_t) of no more than 25% are imparted as well.

Pseudorapidity in the offline selection is confined to $|\eta| < 2.1$, reflecting the geometric boundary of the muon system. The global muon track fit is required to have a minimum of 8 degrees of freedom, as well as a at least 8 hits in the inner tracker. These hits can come from a combination of pixel and strip hits, but at least two hits must come from the pixel detector exclusively. At least 80% of the layers of silicon between the first and last that measure the reconstructed track should have measurements pertaining directly to that track. Further, the global muon track must not exceed a distance of 0.5 cm in either the transverse (xy) or beam (z) directions from its associated primary vertex.

A minimum was placed on the dE/dx estimator ($I_h > 1$ MeV/cm) that is below the average ionization energy deposition of 3 MeV/cm for a speed of light, SM particle. Increasing this minimum would simply reduce the number of SM MIPs stored, but would have no effect on highly ionizing mHSCPs.

Tracker isolation is defined as the sum of transverse momentum from all tracks (excluding the candidate track) within a cone of $\Delta R = \sqrt{\Delta\phi^2 + \Delta\eta^2} < 0.5$ along the candidate track direction, and is restricted to values below 50 GeV. Calorimeter isolation is also possible, but not utilized in the multiply charged analysis. Defined as the ratio of summed HCAL and ECAL energy in a cone of size $\Delta R = \sqrt{\Delta\phi^2 + \Delta\eta^2} < 0.5$ along the global muon track momentum direction to the track momentum, this cut is too sensitive to the scaling of reconstructed momentum with inverse charge, as well as increased energy loss with charge squared for mHSCPs. The effects of applying the various offline selection criteria are given in Fig. 5.1, displaying a steady decrease in efficiency for all signal types as the applied cuts become more rigid.

Table 5.1 displays the effects of applying the global and offline selection criteria in the order of application. The efficiency for data to pass all of the selection for CC and CT both turned on is 0.01273%, and for CC and CT both turned off is 0.01023%.

5.2 Data Quality Improvement

Ionization information is obtained from the tracker strip clusters and pixel detectors. Upon reconstruction, clusters are formed from individual strips with their centroids located at

Table 5.1: Tabulated global and offline selection criterion for the multiply charged analysis as applied to $\sqrt{s} = 13$ TeV data. Cuts are given in order of application, with the relative efficiency in percentage for that cut. Within each cell, the top value corresponds to having both cluster cleaning and cross-talk inversion turned off, while the bottom value corresponds to both cluster cleaning and cross-talk inversion turned on.

Total number of tracks for CC and CT turned off/on: $3.91 \times 10^4/3.93 \times 10^4$

Cut Description	Cut Value	Tracks Passing Cut ($\times 10^4$)	Efficiency (%)
Global Muon Hits in Strip Detector	> 5	3.50 3.49	89.56 88.76
Number of TOF Measurements	> 7	3.50 3.49	100 100
Global Muon Track DOF	> 7	3.33 3.32	95.06 95.10
Global Muon Track Quality	$>= 2$	3.33 3.32	100 100
Global Muon Track χ^2	< 5.0	3.30 3.29	99.28 99.28
Global Minimum p_t (GeV/c)	55.0	1.21 1.20	36.52 36.60
Global Minimum TOF Error (%)	< 15	1.20 $\tilde{1}.20$	99.82 99.76
Global Muon Track Δxy (cm)	< 5	1.20 1.20	100 100
Tracker Isolation (GeV)	< 50	1.03 1.03	85.74 85.88
Relative p_t Error (%)	< 25	1.03 1.03	99.99 99.99
Global Muon Track Δz (cm)	< 5	$\tilde{1}.03$ $\tilde{1}.03$	99.92 99.84
Selection I_{as}	> 0.075	0.0107 0.0198	1.037 1.921
Selection TOF	> 1.125	0.0004 0.0005	3.738 2.525

Overall efficiency with cluster cleaning and cross-talk turned off/on: 0.01023%/0.01273%

the highest-charged (largest signal) strip. Clusters typical of Standard Model particle ionization are ideally characterized by an unsaturated centroid, with Gaussian falloff in the neighboring channels of the cluster. Cluster cleaning and cross-talk inversion are corrective measures that attempt to remove mismeasurement effects caused by non-deal cluster shapes characteristic of mHSCPs.

5.2.1 Cluster Cleaning

Overlapping MIP tracks and nuclear interactions from SM particles in the silicon strips of the tracker can result in undesired ionization contributions. Signal tracks will produce strip clusters with one maximum, with 10% and 4% of the signal being shared with nearest and next-to-nearest neighboring strips, respectively due to cross-talk effects. Cluster cleaning rejects all clusters with multiple charge maxima, as well as those with more than two consecutive strips having both high and comparable charge [31].

5.2.2 Cross-Talk Inversion

Cross-talk inversion exploits the charge/signal distribution in well-behaved signal clusters in order to obtain the correct total energy from those with saturated maxima. Saturated maximas are beyond the dynamic range of the readout electronics, and therefore only a charge threshold can be acquired from direct utilization of the maximum. As described in Sec. 5.2.1, cross-talk effects result in roughly ten percent of the cluster charge being deposited in the direct neighbors of the cluster centroid, and four percent in the next-to-nearest neighbors. The true charge within the saturated centroid can then be determined by taking an average of the the charges given from the 10% and 4% neighbors.

5.3 Background Prediction

As mentioned in Sec. 4.2, simulation is not always perfect in predicting background SM processes. As such, the multiply charged analysis employs a data-driven background prediction method that mitigates potential uncertainties inherent in simulation. The method is predicated on the notion that there exist certain variables which, while uncorrelated for SM background, are correlated for mHSCP signal. Thus, the distribution of data candidates in one region of phase space defined by cuts on these variables can be used to predict the expected number of SM candidates in another region of phase space. This method is known as the ABCD method.

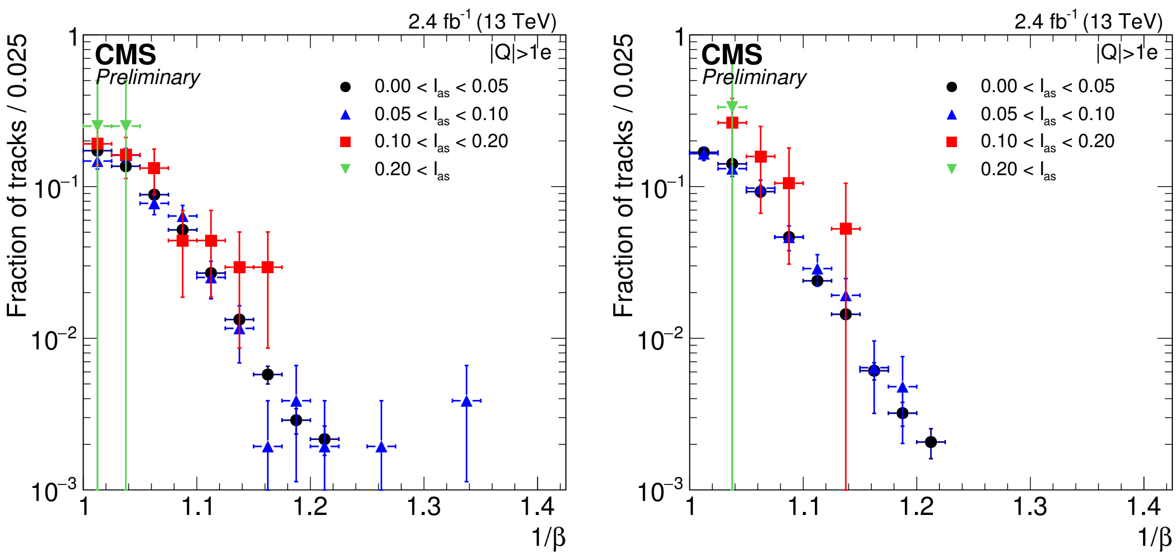

(a) CC CT

(b) None

Figure 5.2: Distributions of $1/\beta$ for varying regions of I_{as} with cluster cleaning and cross-talk applied in the left plot (a) and absent in the right plot (b).

The multiply charged analysis exploits a lack of correlation between time of flight ($1/\beta$) and discriminator (I_{as}) in typical SM particles. Figure 5.2 displays the similarity in form of $1/\beta$ distributions in varying ranges of I_{as}. For each range of discriminator, the $1/\beta$ distributions remain quite similar, within uncertainties. These provide evidence that there is negligible correlation between $1/\beta$ and I_{as} for SM particles. Therefore, time of flight and discriminator serve as suitable variables to use for background prediction. Cuts on each are used to create regions within the $1/\beta - I_{as}$ parameter space, as depicted in Fig. 5.3.

Region A corresponds to the portion of phase space in which the contained data passes neither the time of flight, nor the discriminator cuts. Region B contains data passing the time of flight cut, but not the discriminator cut. Region C contains data passing the discriminator cut, but not the time of flight cut. Region D represents data passing both the time of flight and discriminator cuts, and therefore tentatively the mHSCP signals of interest. Region A is expected to contain virtually nothing but SM background with no mHSCP signal leakage.

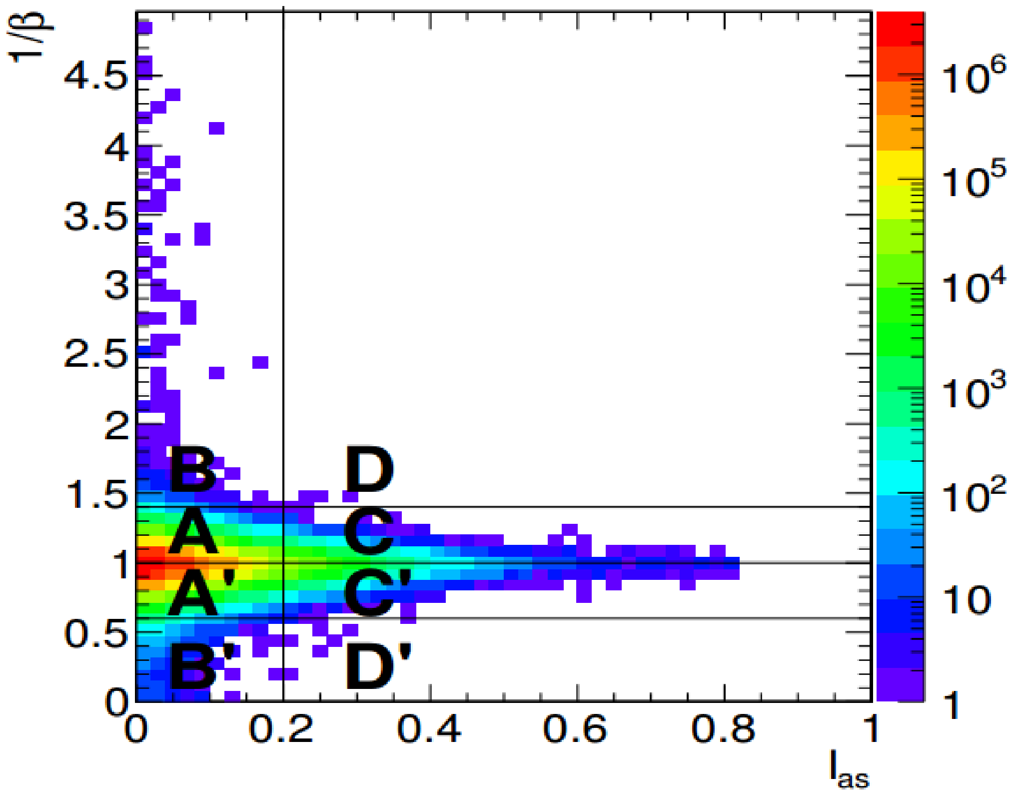

Figure 5.3: Distributions of $1/\beta$ against I_{as} with ABCD regions marked [3].

Due to the lack of correlation between $1/\beta$ and I_{as}, it is true that

$$\frac{N_A}{N_B} \approx \frac{N_C}{N_D}$$
$$N_D \approx \frac{N_A N_B}{N_C} \tag{5.1}$$

where N_i for $i \in \{A, B, C, D\}$ corresponds to the number of SM background measurements in region i. An approximately equal to symbol has been included due to a strict equality being predicated on the notion that there is no signal whatsoever in any of the defined regions. The statistical uncertainty on N_D is given by

$$\sigma_{N_D} = \sqrt{\left(\frac{N_B N_C}{N_A^2}\right)^2 N_A + \left(\frac{N_B}{N_A}\right)^2 N_C + \left(\frac{N_C}{N_A}\right)^2 N_B} \tag{5.2}$$

The number of experimentally observed candidates in region D is then compared to the predicted number from (5.1), where a statistically significant excess could signify the presence of mHSCPs.

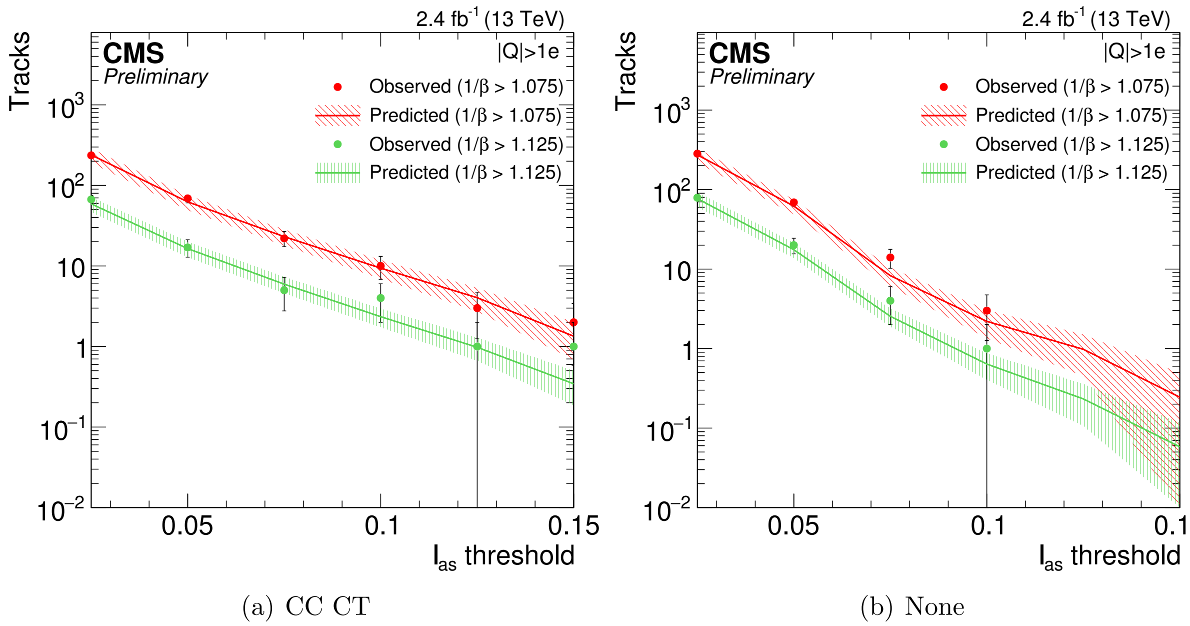

Figure 5.4: Plots of the number of predicted and observed candidates in region D with cluster cleaning and cross-talk turned on in the left plot (a) and off in the right plot (b). Uncertainty includes both statistical (5.2) and systematic (20%) contributions.

To test the validity of the N_D prediction, we apply loose I_{as} and $1/\beta$ cuts to define the ABCD regions, which ensure that all regions are dominated by SM contributions. Predicted and observed candidates are displayed in Fig. 5.4, where acceptable agreement is shown between SM observation and prediction.

6 Results & Conclusions

ABCD method background estimation gives central values of 3 ± 1 and 6 ± 1, and SM particles in the signal region for CC and CT both turned off and on, respectively. These ranges are obtained from the application of statistical and systematic uncertainty (Sec. 5.3) to the predicted values given Table 6.1. The number of observed events present in the signal region falls into the expected range for both CC and CT turned on, and off. Thus, there is no definitive observation of leptonic mHSCPs.

95% confidence level limits on mHSCP cross sections and the effects of cross talk inversion and cluster cleaning are determined. The 95% confidence level cross section limits are summarized in Fig. 6.1, which depicts limits on various cross sections for various charges of mHSCP, as a function of mass. A trend emerges involving the consistent increase of cross section limits with particle charge. The apparent crossing of the charge $8e$ and $9e$ lines is a graphical artifact resulting from a missing 400 GeV/c^2 sample in the analysis. The same results are tabulated in Table 6.2, confirming an increasing cross section for a given mass as charge is increased. The tabulated data also allows for direct comparison between the multiply charged analysis with and without cluster cleaning and cross talk inversion applied.

Consistently, having cluster cleaning and cross-talk inversion activated result in a tighter (lower) limit on the cross section for a mHSCP of a given mass and charge. The sole

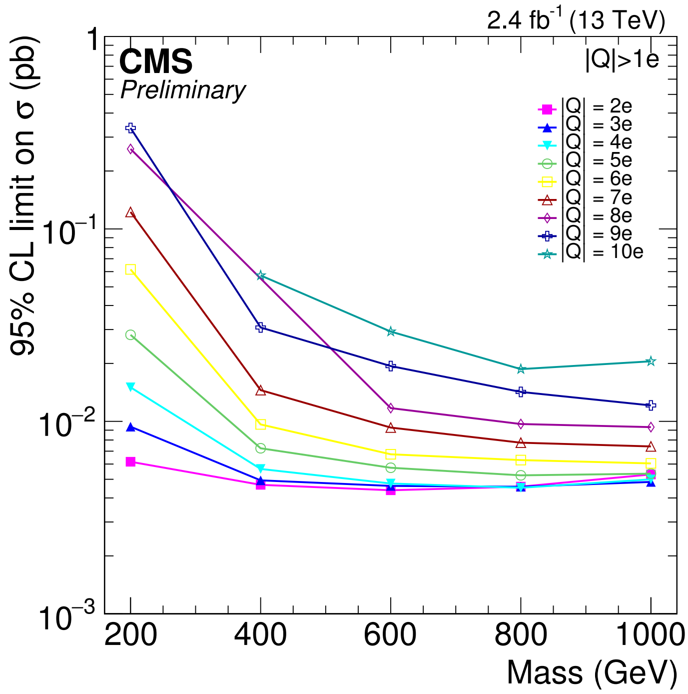

(a) CC CT

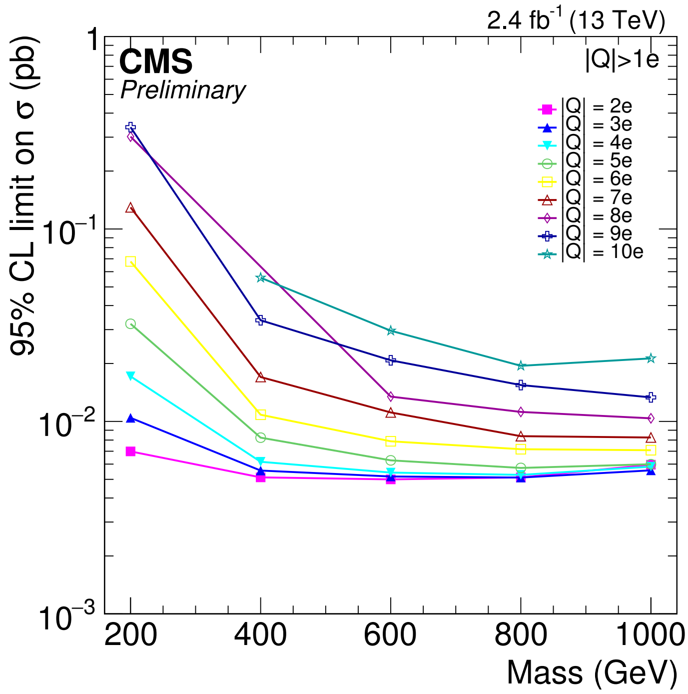

(b) None

Figure 6.1: Plots of observed, 95% confidence level cross section limits on $\sqrt{s} = 13$ TeV mHSCP-like particles. The top plot (a) has both cluster cleaning and cross-talk inversion turned on, while the bottom plot (b) has both turned off.

Table 6.1: Tabulated numbers of observed tracks satisfying I_{as} and $1/\beta$ cuts for various regions pertaining to the ABCD method of section 5.3, using the cuts provided in Table 5.1. The top entry in each cell corresponds to the number of entries observed with both cluster cleaning and cross-talk inversion turned off, while those on the bottom of the cell correspond to having cluster cleaning and cross-talk inversion turned on. The ABCD method predicted number of SM background in region D for CC and CT both off/on are, respectively, 3 and 6 after rounding.

Region	Cut Correspondence	Data in Region
A	$I_{as} < 0.075$ & $1/\beta < 1.125$	4820 4800
B	$I_{as} > 0.075$ & $1/\beta < 1.125$	44 103
C	$I_{as} < 0.075$ & $1/\beta > 1.125$	279 277
D	$I_{as} > 0.075$ & $1/\beta > 1.125$	4 5

mass/charge combination that does not adhere to this trend is the 400 GeV, $q = 10e$ mHSCP. This is likely due to extreme saturation effects that were either not cleaned or inverted properly, or simple statistical fluctuations. Overall, the application of cluster cleaning and cross-talk inversion do improve the analysis in the sense that tighter cross-section limits are placed. Further study into the asymmetric combinations of cleaning and inversion should be conducted to quantify their respective individual effects.

Table 6.2: Experimentally observed 95% confidence level cross section limits for mHSCPs of varying mass and charge. For a given mass and charge combination, the top entry in the cell corresponds to the cross section limit resulting from analysis conducted with no cluster cleaning or cross talk inversion. The bottom entry in a given charge-mass cell corresponds to the analysis with each of the aforementioned turned on. The cross sections are reported in units of fb for readability.

mHSCP Mass (GeV/c^2)	mHSCP Charge								
	$2e$	$3e$	$4e$	$5e$	$6e$	$7e$	$8e$	$9e$	$10e$
200 GeV/c^2	6.986 6.168	10.440 9.384	17.150 15.029	32.160 28.162	67.798 61.613	129.543 122.503	301.977 260.343	337.976 334.539	N/A N/A
400 GeV/c^2	5.120 4.680	5.555 4.937	6.170 5.685	8.235 7.247	10.834 9.640	17.011 14.530	N/A N/A	33.551 30.758	55.805 57.320
600 GeV/c^2	4.998 4.385	5.174 4.619	5.422 4.754	6.276 5.740	7.884 6.744	11.133 9.285	13.456 11.719	20.775 19.379	29.602 29.277
800 GeV/c^2	5.119 4.579	5.109 4.574	5.275 4.519	5.732 5.243	7.171 6.292	8.382 7.747	11.204 9.686	15.452 14.222	19.456 18.687
1000 GeV/c^2	5.958 5.299	5.569 4.845	5.821 4.996	5.993 5.348	7.086 6.047	8.250 7.409	10.379 9.334	13.334 12.102	21.256 20.512

Bibliography

[1] T. P. Cheng and L. F. Li. *GAUGE THEORY OF ELEMENTARY PARTICLE PHYSICS*. 1984.

[2] M. Fairbairn et al. "Stable massive particles at colliders". In: *Phys. Rept.* 438 (2007), pp. 1–63. DOI: 10.1016/j.physrep.2006.10.002. arXiv: hep-ph/0611040 [hep-ph].

[3] Venkatesh Veeraraghavan. "Search for multiply charged Heavy Stable Charged Particles in data collected with the CMS detector." PhD thesis. Florida State U., 2013. URL: http://lss.fnal.gov/archive/thesis/2000/fermilab-thesis-2013-25.pdf.

[4] Loic Quertenmont. "Search for Heavy Stable Charged Particles with the CMS detector at the LHC". In: *Proceedings, 20th International Workshop on Deep-Inelastic Scattering and Related Subjects (DIS 2012).* 2012, pp. 625–628. DOI: 10.3204/DESY-PROC-2012-02/223.

[5] M. Drees and X. Tata. "Signals for heavy exotics at hadron colliders and supercolliders". In: *Physics Letters B* 252.4 (1990), pp. 695–702. ISSN: 0370-2693. DOI: http://dx.doi.org/10.1016/0370-2693(90)90508-4. URL: http://www.sciencedirect.com/science/article/pii/0370269390905084.

[6] Alexander Kusenko and Mikhail Shaposhnikov. "Supersymmetric Q-balls as dark matter". In: *Physics Letters B* 418.1–2 (1998), pp. 46–54. ISSN: 0370-2693. DOI:

http://dx.doi.org/10.1016/S0370-2693(97)01375-0. URL: http://www.sciencedirect.com/science/article/pii/S0370269397013750.

[7] Vardan Khachatryan et al. "Search for supersymmetry in the multijet and missing transverse momentum final state in pp collisions at 13 TeV". In: (2016). arXiv: 1602.06581 [hep-ex].

[8] Christiane Lefèvre. "The CERN accelerator complex. Complexe des accélérateurs du CERN". Dec. 2008. URL: https://cds.cern.ch/record/1260465.

[9] Lyndon Evans and Philip Bryant. "LHC Machine". In: *JINST* 3 (2008), S08001. DOI: 10.1088/1748-0221/3/08/S08001.

[10] Oliver S. Bruning et al. "LHC Design Report Vol.1: The LHC Main Ring". In: (2004).

[11] S. Chatrchyan et al. "The CMS experiment at the CERN LHC". In: *JINST* 3 (2008), S08004. DOI: 10.1088/1748-0221/3/08/S08004.

[12] G. Aad et al. "The ATLAS Experiment at the CERN Large Hadron Collider". In: *JINST* 3 (2008), S08003. DOI: 10.1088/1748-0221/3/08/S08003.

[13] CMS Collaboration. *CMS DETECTOR*. 2012. URL: https://cms-docdb.cern.ch/cgi-bin/PublicDocDB/RetrieveFile?docid=11514&version=1&filename=cms_120918_03.png.

[14] C.Y. Wong. *Introduction to High-energy Heavy-ion Collisions*. Introduction to High-energy Heavy-ion Collisions. World Scientific, 1994. ISBN: 9789810202637. URL: https://books.google.com/books?id=Fnxvrdj2NOQC.

[15] S Chatrchyan et al. "Performance of the CMS Drift Tube Chambers with Cosmic Rays". In: *JINST* 5 (2010), T03015. DOI: 10.1088/1748-0221/5/03/T03015. arXiv: 0911.4855 [physics.ins-det].

[16] CMS Collaboration. *CMS Detector Drawings*. 2012. URL: https://cms-docdb.cern.ch/cgi-bin/PublicDocDB/RetrieveFile?docid=5955&filename=cms_complete_labelled.pdf&version=1.

[17] Manfred Krammer. "The silicon sensors for the Inner Tracker of the Compact Muon Solenoid experiment". In: *Nucl. Instrum. Methods Phys. Res., A* 531 (2004), pp. 238–245. URL: http://cds.cern.ch/record/816579.

[18] Serguei Chatrchyan et al. "Alignment of the CMS tracker with LHC and cosmic ray data". In: *JINST* 9 (2014), P06009. DOI: 10.1088/1748-0221/9/06/P06009. arXiv: 1403.2286 [physics.ins-det].

[19] A. Giammanco. "Particle identification with energy loss in the CMS silicon strip tracker". In: (2007).

[20] Erik Butz. "Calibration, alignment and long-term performance of the CMS silicon tracking detector". PhD thesis. Hamburg U., 2009. DOI: 10.3204/DESY-THESIS-2009-008. URL: http://www-library.desy.de/cgi-bin/showprep.pl?thesis09-008.

[21] Alessio Ghezzi. "The CMS electromagnetic calorimeter calibration during Run I: progress achieved and expectations for Run II". In: *J. Phys. Conf. Ser.* 587.1 (2015), p. 012002. DOI: 10.1088/1742-6596/587/1/012002.

[22] "CMS: The hadron calorimeter technical design report". In: (1997).

[23] CMS Collaboration. "CMS, the Compact Muon Solenoid. Muon technical design report". In: (1997).

[24] Serguei Chatrchyan et al. "Performance of CMS muon reconstruction in *pp* collision events at $\sqrt{s} = 7$ TeV". In: *JINST* 7 (2012), P10002. DOI: 10.1088/1748-0221/7/10/P10002. arXiv: 1206.4071 [physics.ins-det].

[25] F. James. *Statistical Methods in Experimental Physics*. World Scientific Publishing, 2006. ISBN: 9789812705273. URL: https://books.google.com/books?id=S8N%5C_QgAACAAJ.

[26] Serguei Chatrchyan et al. "Searches for long-lived charged particles in pp collisions at $\sqrt{s}$=7 and 8 TeV". In: *JHEP* 07 (2013), p. 122. DOI: 10.1007/JHEP07(2013)122. arXiv: 1305.0491 [hep-ex].

[27] CMS Collaboration. "Searches for Long-lived Charged Particles in Proton-Proton Collisions at $\sqrt{s} = 13$ TeV". In: (2015). URL: http://inspirehep.net/record/1409816.

[28] J. Beringer et al. "Review of Particle Physics*". In: *Phys. Rev. D* 86 (1 July 2012), p. 010001. DOI: 10.1103/PhysRevD.86.010001. URL: http://link.aps.org/doi/10.1103/PhysRevD.86.010001.

[29] Torbjorn Sjostrand, Stephen Mrenna, and Peter Z. Skands. "PYTHIA 6.4 Physics and Manual". In: *JHEP* 05 (2006), p. 026. DOI: 10.1088/1126-6708/2006/05/026. arXiv: hep-ph/0603175 [hep-ph].

[30] S. Agostinelli et al. "GEANT4: A Simulation toolkit". In: *Nucl. Instrum. Meth.* A506 (2003), pp. 250–303. DOI: 10.1016/S0168-9002(03)01368-8.

[31] *Search for Heavy Stable Charged Particles in pp collisions at 7 TeV*. Tech. rep. CMS-PAS-EXO-10-004. 2010. Geneva: CERN, 2010. URL: http://cds.cern.ch/record/1280690.